

Bridgmanite-Predominant Lower Mantle Evidenced from Velocity and Density Profiles across the 660-km Discontinuity

Suyu Fu

The University of Texas at Austin <https://orcid.org/0000-0002-8837-3957>

Yanyao Zhang

The University of Texas at Austin

Takuo Okuchi

Okayama University

Jung-Fu Lin (✉ afu@jsg.utexas.edu)

The University of Texas at Austin <https://orcid.org/0000-0002-0163-5329>

Article

Keywords: Earth, mantle, bridgmanite

Posted Date: January 29th, 2021

DOI: <https://doi.org/10.21203/rs.3.rs-154057/v1>

License:  This work is licensed under a Creative Commons Attribution 4.0 International License.

[Read Full License](#)

Bridgmanite-Predominant Lower Mantle Evidenced from Velocity and Density Profiles across the 660-km Discontinuity

Suyu Fu^{1,*}, Yanyao Zhang¹, Takuo Okuchi², Jung-Fu Lin^{1,*}

¹Department of Geological Sciences, Jackson School of Geosciences, The University of Texas at Austin, Austin, TX, USA

²Institute for Planetary Materials, Okayama University, Misasa, Japan

*Corresponding author: Jung-Fu Lin (afu@jsg.utexas.edu), Suyu Fu (fsyxhy@gmail.com)

Abstract (Nature Communications style <150 words)

Earth's mantle composition is essential to our understanding of its physics and dynamics. Here we report single-crystal elasticity (C_{ij}) of (Al,Fe)-bearing bridgmanite, $\text{Mg}_{0.88}\text{Fe}_{0.1}\text{Al}_{0.14}\text{Si}_{0.90}\text{O}_3$ with $\text{Fe}^{3+}/\sum\text{Fe}\sim 0.65$, up to ~ 82 GPa measured in diamond anvil cells. Together with heat capacity measurements on bridgmanite and ferropericlase, we develop a fully internally-consistent thermoelastic model to simultaneously evaluate lower-mantle mineralogy and geotherm via comparisons of P-wave, S-wave velocities, and density (V_P , V_S , and ρ) with one-dimensional seismic profiles. Our best-fit model demonstrates the lower mantle consists of ~ 89 vol% (Al,Fe)-bearing bridgmanite, ~ 4 vol% ferropericlase, and ~ 7 vol% CaSiO_3 perovskite. A chemically layered mantle with pyrolitic upper mantle and bridgmanite-predominant lower mantle would display $\sim 3.2(\pm 1.5)\%$, $\sim 5.2(\pm 1.5)\%$, and $\sim 5.0(\pm 1.0)\%$ jumps in V_P , V_S , and ρ , respectively, across the 660-km discontinuity, which are well consistent with seismic reflection observations. The lower mantle could have become bridgmanite-predominant via accumulations of ancient silica-rich materials, which helps explain current deep-Earth seismic and geochemical signatures.

Introduction

Strong seismic reflections at 660-km depth, marked by sharp velocity and density jumps¹⁻⁶, have long been associated with a structural transition from ringwoodite to bridgmanite and ferropericlase⁷. Geochemical and petrological observations indicate that Earth's upper mantle likely consists of pyrolite⁸ with approximately three portions of peridotite and one portion of basalt, although some studies also proposed a garnet-rich piclogite in the transition zone⁹. If one assumes the whole mantle is chemically homogenous in major elements, a pyrolitic lower mantle would have ~75 vol% (Al,Fe)-bearing bridgmanite [(Mg,Fe,Al),(Fe,Al,Si)O₃, Bgm], ~18 vol% ferropericlase [(Mg,Fe)O, Fp], and ~7 vol% CaSiO₃ perovskite¹⁰. However, studies show that structural transition(s) alone in pyrolite cannot simply explain the aforementioned velocity and density jumps at 660-km depth^{3,11}. A recent seismic study observed regional small-scale topography along the 660-km boundary, implying a discontinuous chemical layer across the region¹². Moreover, such a pyrolitic model with Mg/Si~1.25 has much less Si than the chondritic bulk Earth model¹³ with Mg/Si~1.0. To address the “missing Si” conundrum in the silicate Earth, Si as a light element in the core¹⁴ and/or a Si-rich lower mantle¹⁵ have been proposed previously. Thus far, the first-order question on the mantle mineralogy remains as to whether or not the 660-km discontinuity represents a structural transition as well as a chemical boundary. In other words, is the mantle chemically homogeneous or layered into upper and lower mantles?

Velocity and density comparisons between seismic observations^{1,2} and mineral physics models^{10,16-18} have been widely used to provide insights into the mantle mineralogy. Of particular example is the study by Murakami et al.¹⁷, which used V_s of polycrystalline Al-bearing bridgmanite up to 124 GPa and 2700 K to suggest a perovskitic lower mantle with greater than 93 vol% bridgmanite. However, it has been pointed out by Cottaar et al.¹⁹ that the conclusion of a

perovskitic lower mantle¹⁷ was not supported because of using inconsistent thermoelastic modeling and inappropriate averaging schemes for mineral aggregates. A recent study¹⁶ extended aggregate V_P and V_S of (Al,Fe)-bearing bridgmanite, $Mg_{0.9}Fe_{0.1}Al_{0.1}Si_{0.9}O_3$ (Fe10-Al10-Bgm), up to 40 GPa at room temperature from single-crystal elasticity measurements and suggested a Fe^{3+} -rich pyrolitic lower mantle above 1200-km depth. Nevertheless, further analyses²⁰ revealed different velocity profiles and large uncertainties of the reported elasticity¹⁶ as a result of using insensitive crystal platelets with limited high-pressure V_P data. To make matters worse, velocity and density profiles of candidate minerals in these studies^{10,16-18} were typically modeled along a previously reported geotherm²¹⁻²⁴, a pressure-temperature (P-T) profile of the mantle. For instance, Katsura et al.²² assume the whole mantle is dominated by heat convection and calculate an adiabatic geotherm for pyrolite with a temperature gradient: $(\partial T/\partial P)_S = \alpha T/\rho C_P$, where T is the temperature at a certain depth/pressure, and α , ρ , and C_P are thermal expansion coefficient, density, and isobaric heat capacity of constituent materials, respectively. Building a consistent mantle geotherm would thus require quantitative knowledge of its mineralogy and respective high P-T thermoelastic properties. In a nutshell, because of the lack of a complete dataset on extended V_P , V_S , ρ , and C_P properties with small uncertainties and a fully internally-consistent thermoelastic model on geotherm, we could not unambiguously constrain the lower-mantle mineralogy and associated Mg/Si, and understand seismic and dynamic signatures across the 660-km boundary.

Here we reliably determined single-crystal elasticity (C_{ij}) of (Al,Fe)-bearing bridgmanite, $Mg_{0.88}Fe_{0.1}Al_{0.14}Si_{0.90}O_3$ (Fe10-Al14-Bgm) with $Fe^{3+}/\sum Fe \sim 0.65$, up to ~ 82 GPa at 300 K using impulsive stimulated light scattering (ISLS), Brillouin light scattering (BLS), and synchrotron X-ray diffraction (XRD) in diamond anvil cells (DACs) (Methods, see detailed sample characterizations in a literature²⁵). Two platelets with crystallographic orientations of (-0.50, 0.05,

-0.86) and (0.65, -0.59, 0.48) are selected with sufficient sensitivities to derive full C_{ij} with small uncertainties (Fig. 1a-b). The use of both ISLS and BLS^{26,27} enables reliable V_P and V_S measurements on selected platelets as a function of azimuthal angles, and XRD results provide the relevant pressure-density relationship (Fig. 1c-e, Supplementary Table 1, and Supplementary Fig. 1). This combined approach in data collection and analyses overcomes previous difficulties^{16,17} in obtaining V_P of bridgmanite above 20 GPa when only using BLS. Furthermore, we measured ambient-pressure C_P of polycrystalline $\text{Mg}_{0.96}\text{Fe}_{0.05}\text{Si}_{0.99}\text{O}_3$ bridgmanite with $\text{Fe}^{3+}/\sum\text{Fe}\approx 0.28$ and $\text{Mg}_{0.8}\text{Fe}_{0.2}\text{O}$ ferropericlasite at 2-300 K and 300-400 K, respectively, using a physical property measurement system (Methods, Fig. 1f-g, and Supplementary Table 2). These thermoelastic data of bridgmanite and ferropericlasite as well as literature reports for CaSiO_3 perovskite²⁸ are evaluated altogether using a fully internally-consistent thermoelastic model²⁹ within the framework of Mie-Grüneisen thermal equation of state (EoS) and finite-strain theory to provide multiple physical constraints on lower-mantle mineralogy and geotherm.

Results

Figure 1c-e shows representative BLS and ISLS spectra with high signal-to-noise ratios to derive V_{S1} , V_{S2} , and V_P of single-crystal Fe10-Al14-Bgm at ~82 GPa. Furthermore, measured C_P of Fe-bearing bridgmanite as a function of temperature are consistent with literature reports^{30,31} of MgSiO_3 bridgmanite within uncertainties (Fig. 1f-g). This indicates that Fe substitution has a negligible effect on C_P of bridgmanite. The modeled high P-T C_P of bridgmanite as well as ferropericlasite agree well with *ab initio* calculations^{32,33}.

Collected velocities with rotations of the DAC about its compression axis over a range of 200° were fit using Christoffel's equations³⁴ to derive its full C_{ij} at each experimental pressure (Supplementary Figs. 2-3). Results show that all C_{ij} increase monotonically with pressure up to 82

GPa with uncertainties of 1-2%, except C_{55} and C_{23} with errors of ~3-4% (Supplementary Tables 3-4). In particular, the derived C_{ij} of Fe10-Al14-Bgm at 25 and 35 GPa are comparable to those of literature single-crystal bridgmanite³⁵⁻³⁷. We note that the slight difference on pressure derivatives of C_{ij} between this study and *ab initio* calculations for MgSiO₃ bridgmanite³⁸⁻⁴⁰ might come from compositional differences and/or limitations of theoretical simulations. Calculated aggregate V_S and V_P of single-crystal Fe10-Al14-Bgm show uncertainties less than 1.0% using a Voigt-Reuss-Hill averaging scheme⁴¹ (Methods).

Our results show that aggregate V_S and V_P of single-crystal Fe10-Al14-Bgm increase monotonically with pressure up to ~82 GPa (Fig. 2). Literature studies indicate that lower-mantle bridgmanite could accommodate abundant Fe³⁺ and Al³⁺ to replace dodecahedral-site (A-site) Mg²⁺ and octahedral-site (B-site) Si⁴⁺ via charge-coupled substitution⁴². B-site Fe³⁺ in Fe-bearing bridgmanite is reported to undergo a spin transition at approximately 40-60 GPa, which is associated with an abrupt V_P softening²⁶. Our bridgmanite, Mg_{0.88}Fe_{0.1}Al_{0.14}Si_{0.90}O₃, contains 14% Al preferentially in the B site and ~10% Fe mostly in the A site. Thus, the sample is not expected to undergo a spin transition and will display a monotonic increase in V_S and V_P with pressure. Additionally, we note that the room-temperature V_S and V_P of bridgmanite are much higher than those of ferropericlase^{27,43} and CaSiO₃ perovskite²⁸.

Discussion

Here, we have developed a fully internally-consistent thermoelastic model to simultaneously evaluate lower-mantle mineralogy and temperature profile. In this model, we assume that the lower mantle, to the first order, is chemically homogenous, adiabatic, and under gravitational self-compression with Bullen's parameter close to one because of the consistency between 1D seismic profiles^{1,2} and the Adams-Williamson equation⁴⁴ (see Methods for details).. Third-order Eulerian

finite-strain equations²⁹ and Mie-Grüneisen EoS are adopted to model high P-T thermoelastic properties of bridgmanite, ferropericlase, and CaSiO₃ perovskite, including V_P , V_S , ρ , α , and C_P (Supplementary Tables 5-6, Supplementary Figs. 4-7). We have also considered effects of the spin crossover in ferropericlase^{27,43} as well as Fe partitioning (K_D) between bridgmanite and ferropericlase in the lower mantle¹⁰. To quantitatively evaluate Fe and Al substitution effects on the velocity and density of bridgmanite, experimental data from this study and the literature^{16,17,45-47} are fit together to derive the adiabatic bulk (shear) modulus, K_{S0} (μ_0), and its pressure derivative, K'_{S0} (μ'_0), as a function of Fe and Al contents. Moreover, considering the frequency dependence of seismic attenuation⁴⁸, corrections from experimental high-frequency data (~GHz) to seismic frequencies (~Hz) are also conducted for modeled velocity profiles (Methods, Supplementary Fig. 8). The amount of CaSiO₃ perovskite is fixed as 7 vol% because its abundance in both pyrolitic and chondritic models¹³ is about 5-10 vol%. With all these parameters taken into consideration, we initially use a pyrolitic lower-mantle mineralogy as a reference to evaluate V_P , V_S , and ρ profiles of the three major minerals along an adiabatic geotherm. Considering trade-offs between compositional and thermal parameters, an iterative procedure with uncertainty minimization is conducted until the best-fit model converges with PREM profiles¹.

In our best-fit model, bridgmanite displays slightly higher velocities than those of PREM, while ferropericlase and CaSiO₃ perovskite show lower velocities (Fig. 2c-d and Supplementary Fig. 9). In particular, V_S of these three minerals are well distinguishable from one another after taking uncertainties into account, that makes it the most sensitive elastic parameter to evaluate the lower-mantle mineralogy. V_P softening across the spin crossover in ferropericlase is smeared out but still visible at mid-lower mantle P-T. Notably, the spin crossover in ferropericlase increases its Fe content in the low-spin state¹⁰, which in turn flattens V_S toward the deeper lower mantle. We

note that if K_D is constant with depth, V_s of ferropericlasite increases monotonically in the lower mantle (Supplementary Fig. 9g-i).

Our best fits to PREM¹ show a lower-mantle mineralogy of $\sim 88.7(\pm 2.0)$ vol% (Al,Fe)-bearing bridgmanite, $\sim 4.3(\pm 2.0)$ vol% ferropericlasite, and 7 vol% (fixed) CaSiO₃ perovskite (Fig. 3), thereafter called the bridgmanite-predominant lower-mantle model. In contrast, a pyrolitic model shows lower V_P and V_S than those of PREM, whereas ρ profiles between pyrolitic and bridgmanite-predominant models are indistinguishable. With an adiabatic lower-mantle convection⁴⁴, the derived geotherm ranges from 1920 K at 660-km depth, an anchor potential temperature for the post-spinel phase transformation⁷, to 2560(± 80) K at 2800-km depth. Our best-fit geotherm is comparable with that for a chondritic composition from *ab initio* calculations²⁴. On the other hand, if we assume the lower mantle is superadiabatic^{44,49} with Bullen's parameter of ~ 0.8 , the superadiabatic geotherm will be ~ 300 K higher than our best-fit adiabat at ~ 2800 -km depth. It should be noted that such a superadiabatic geotherm will consequently result in significant velocity mismatches with PREM in both bridgmanite-predominant and pyrolitic models. To further test the sensitivity of K_D and the amount of CaSiO₃ perovskite to our modeled results, we allow them to vary within a reasonable compositional range and find that variations in these two parameters have limited effects on the derived lower-mantle mineralogy (e.g., they would cause ~ 2 vol% variation in bridgmanite content) and $< 0.5\%$ in geotherm (Supplementary Fig. 10 and Supplementary Table 7). We note that the anelastic relaxation correction from \sim GHz to \sim Hz slightly decreases modeled velocity profiles by $\sim 0.3\%$; without such a correction, the modelled velocity profiles would be more similar to a pyrolitic composition (less bridgmanite) in the lower mantle.

It is important to analyze uncertainties of these modeled results before one can reach a firm conclusion on the mantle mineralogy and geotherm. Using standard error propagations, our

modeled high P-T V_P , V_S , and ρ profiles typically have uncertainties of $\pm 2.2\%$, $\pm 1.8\%$, and $\pm 1.1\%$, respectively, at $\pm 1\sigma$ level (see Methods). A pyrolitic model¹⁰ with $+1\sigma$ upper bounds would marginally overlap with PREM profiles¹ and display an adiabatic geotherm ~ 100 K higher than our best-fit model at ~ 2800 -km depth (Fig. 3). Alternatively, if the chosen anchor potential temperature at 660-km depth decreases by ~ 500 K to ~ 1420 K, a pyrolitic model could also match PREM well. We note that this temperature reduction might be too large to be realistic at the topmost lower mantle according to literature reports on post-spinel and/or post-garnet transformations⁷. Overall, with the most comprehensive thermoelastic study on major lower-mantle minerals along an adiabatic geotherm to date, our results indicate bridgmanite is the most predominant mineral ranging from ~ 75 to ~ 100 vol% after taking $\pm 1\sigma$ uncertainties into account.

Analyses of seismic reflections at 660-km depth³⁻⁶ have shown significant velocity and density jumps with $\Delta V_P/V_P$, $\Delta V_S/V_S$, and $\Delta \rho/\rho$ of $\sim 2.0(\pm 0.7)\%$, $\sim 4.8(\pm 1.9)\%$, and $\sim 5.2(\pm 0.3)\%$, respectively. Magnitudes of these jumps are closely related to structural and possibly compositional transitions across the boundary and thus can provide additional constraints on the mantle mineralogy. If we assume the mantle is chemically layered with a pyrolitic transition zone⁸ and bridgmanite-predominant lower mantle, the calculated $\Delta V_P/V_P$, $\Delta V_S/V_S$, and $\Delta \rho/\rho$ jumps across the 660-km boundary are $\sim 3.2(\pm 1.5)\%$, $\sim 5.2(\pm 1.5)\%$, and $\sim 5.0(\pm 1.0)\%$, respectively (Fig. 4 and Supplementary Figs. 11-12). These values are well consistent with seismic reflection observations³⁻⁶, falling within 1σ confidence ellipses. In comparison, we further consider three scenarios by assuming a chemically homogeneous whole mantle: (1) peridotite⁵⁰ with a harzburgite composition of $\text{Mg/Si} \sim 1.5$ (~ 80 vol% ringwoodite and ~ 20 vol% majorite); (2) pyrolite⁸ with $\text{Mg/Si} \sim 1.25$ (~ 60 vol% ringwoodite and ~ 40 vol% majorite); (3) piclogite⁹ with $\text{Mg/Si} \sim 0.9$ (~ 20 vol% ringwoodite and ~ 80 vol% majorite). Our calculations show that phase

transformations in these models produce jumps that are not consistent with seismic reflection observations³⁻⁶. For instance, the peridotite model displays $\sim 3.3(\pm 0.5)\%$ in $\Delta V_P/V_P$, $\sim 7.6(\pm 0.5)\%$ in $\Delta V_S/V_S$, and $\sim 9.0(\pm 0.3)\%$ in $\Delta \rho/\rho$, while the piclogite model⁹ would increase $\Delta V_P/V_P$ and $\Delta V_S/V_S$ to $\sim 4.6(\pm 1.0)\%$ and $\sim 8.6(\pm 1.0)\%$, respectively, and decrease $\Delta \rho/\rho$ to $\sim 5.8(\pm 0.8)\%$. We note that early studies⁵¹ suggest potential mantle differentiation could result in physical mixing of multiple lithologies. We have used peridotite and piclogite as end members to evaluate physical mixtures with different lithology percentages, but their velocity and density jumps are still not comparable with seismically-observed discontinuities at the 660-km depth³⁻⁶. In summary, these analyses provide supportive evidence for a chemically layered mantle with a bridgmanite-predominant lower mantle and pyrolitic upper mantle.

Our bridgmanite-predominant lower-mantle model is silica-rich with $\text{Mg/Si} \sim 0.97$. Assuming a pyrolitic upper mantle with $\text{Mg/Si} \sim 1.25$, the Mg/Si for bulk silicate Earth will be about 1.05. The bulk Earth is generally believed to be chondritic¹³ with $\text{Mg/Si} \sim 1$, despite some geochemical evidence challenging such a model⁵². The bridgmanite-predominant lower mantle is consistent with the chondritic bulk Earth model¹⁵ by having more “missing Si” in the lower mantle. Furthermore, the chemically layered mantle can have ramifications on dynamic processes of our planet. Seismic tomography shows that some subducting slabs can penetrate through the transition zone into the lower mantle to help homogenize mantle chemistry in a whole-mantle convection model. In contrast, stagnant slabs are found to be prevalent in the transition zone⁵³, that might indicate a layered-mantle convection model. Bridgmanite is suggested to be ~ 1000 times rheologically stronger than ferropericlasite⁵⁴. The bulk viscosity for a bridgmanite-predominant lower mantle is estimated to be 1-2 orders higher than previously thought for a pyrolitic lower mantle⁵⁵ (Supplementary Fig. 13). A recent geodynamic study⁵⁵ proposed that ancient Si-rich

materials in the lower mantle would behave sufficiently rigid to resist whole-mantle mixing, which helps maintain chemical layering over 4.6 Gyr of Earth's evolution. In the meanwhile, conduits and channels could exist between these rigid ancient blobs⁵⁵ to allow regional penetrations of subducting slabs into the lower mantle. Due to high viscosity of the bridgmanite-predominant lower mantle, some cold slabs could remain metastable and seismically visible with the slow mechanical mixing. Early studies indicate that such highly viscous convecting materials in the lower mantle might make it slightly superadiabatic²¹. Considering the mantle adiabaticity estimated from seismic profiles^{1,44} and other potential contributions⁴⁹, such as internal heating, future studies using combined high-quality mineral physics and high-resolution seismic data are needed to elucidate spatial and temporal signatures of the mantle geophysics and geochemistry.

Acknowledgements

The authors acknowledge S. Grand, I. Jackson and C. Liu for constructive discussions, and J. Zhou, Z. Li, and J. Gao for heat capacity measurements on polycrystalline bridgmanite and ferropericlase. The authors appreciate V. Prakapenka and E. Greenberg for helping with X-ray diffraction experiments at 13ID-D, GSECARS. GSECARS was supported by the National Science Foundation (EAR-1128799) and U.S. Department of Energy, Geosciences (DE-FG02-94ER14466). J.F. Lin acknowledges support from National Science Foundation Geophysics Program (EAR-1446946 & EAR-1916941) and the Joint Use/Research Program of the Institute for Planetary Materials, Okayama University. T. Okuchi acknowledges support from JSPS KAKENHI (17H01172).

Author contributions

S.F. and J.F.L. designed the research. J.F.L. and T.O. synthesized the starting sample. S.F. and Y.Z. conducted high-pressure BLS, ISLS, and XRD experiments. S.F. analyzed the data and performed the modelling. S.F. and J.F.L. wrote the manuscript draft, and all authors discussed and commented on the content of the manuscript.

Materials & Correspondence

Supplementary information is available. Correspondence and requests for materials should be addressed to J.F.L. (afu@jsg.utexas.edu) and S.F. (fsyxhy@gmail.com).

Competing interests

The authors declare no competing interests.

Methods

Sample synthesis and characterizations. Single-crystal bridgmanite with run number 5K2667 were synthesized using the 5000-ton Kawai-type multi-anvil apparatus at the Institute for Planetary Materials at Okayama University. Starting materials of magnesium hydroxide [Mg(OH)₂], enstatite [MgSiO₃], aluminum oxide [Al₂O₃], and iron oxide [⁵⁷FeO] were mechanically mixed with desired weight percentages, and were then sealed into a Pt capsule. The Pt capsule were compressed and heated up to ~24 GPa and ~1800 °C for 20 h to synthesize high-quality single-crystal (Al,Fe)-bearing bridgmanite. Details of sample synthesis and characterizations on its chemistry, Fe³⁺/ΣFe, and crystallinity have been well documented in a literature study²⁵. Results from electron microprobe analysis, Mössbauer spectroscopy, Raman spectroscopy, transmission

electron microscopy, and synchrotron XRD show that the synthesized bridgmanite is chemically homogeneous and inclusions-free in micrometer- to nanometer-spatial resolutions with a composition of $\text{Mg}_{0.88}\text{Fe}_{0.1}\text{Al}_{0.14}\text{Si}_{0.90}\text{O}_3$ (Fe10-Al14-Bgm, $\text{Fe}^{3+}/\Sigma\text{Fe} \approx 0.65$) and ambient lattice parameters of $a = 4.7875(3) \text{ \AA}$, $b = 4.9423(2) \text{ \AA}$, $c = 6.9205(6)$.

Selection of single-crystal platelets to derive its full C_{ij} . Bridgmanite has an orthorhombic structure ($Pbnm$) in lower-mantle conditions with nine independent C_{ij} to be constrained. Following a literature procedure³⁵, we first double-side polished several platelets to $\sim 25\text{-}30 \mu\text{m}$ thick using 3M diamond film and conducted synchrotron single-crystal XRD at ambient conditions at 13ID-D GeoSoilEnviroCARS (GSECARS) of the Advanced Photon Source (APS), Argonne National Laboratory (ANL) using an incident X-ray with a 0.3344-\AA wavelength. $\pm 15^\circ$ rotations of each platelet about the vertical axis of the sample stage were employed to reliably determine its crystallographic orientation. Then, we calculated the sensitivity of synthetic velocities to C_{ij} in each specific orientation so that we can select appropriate platelets that can be used to derive full C_{ij} with small uncertainties. Based on these analyses (Fig. 1a-b), two platelets with orientations of $(-0.50, 0.05, -0.86)$ and $(0.65, -0.59, 0.48)$ with sufficient sensitivities are used for further velocity measurements.

High-pressure velocity and density measurements. BLS and ISLS measurements were conducted on selected platelets up to 82 GPa with a pressure interval of 6-10 GPa in the Mineral Physics Laboratory of the Department of Geological Sciences at The University of Texas at Austin. Re gaskets with initial thicknesses of $250 \mu\text{m}$ were pre-indented to 25 GPa or $\sim 28\text{-}\mu\text{m}$ thick using a short symmetric $200\text{-}\mu\text{m}$ -culet DAC. Pre-indented areas were drilled with $130\text{-}\mu\text{m}$ diameter holes as sample chambers. Selected platelets were cut using focused ion beam into circular shapes, $\sim 60\text{-}70 \mu\text{m}$ in diameter, and polished down to $10 \mu\text{m}$ thick to be loaded into sample chambers in

two runs. Neon was used as pressure medium and a ruby sphere pressure calibrant was placed close to the sample to minimize pressure uncertainties (Fig. 1c insert). We note that, to achieve equilibrium and ensure pressure consistency between two runs, each DAC was kept at the target experimental pressure for 2-3 days before each measurement. Ruby fluorescence was taken before and after velocity measurements to evaluate pressure and pressure uncertainties⁵⁶. We use the ruby pressure scale by Dewaele et al.⁵⁶ because of its internal consistency with the Au pressure scale used in our complementary XRD experiments.

The BLS system is equipped with a solid-state green laser of 532-nm wavelength (Coherent Verdi V2), an APD detector (Laser Components Count-10B), and a JRS six-pass tandem Fabry-Perot Interferometer. BLS spectra were collected at a forward scattering geometry with an external scattering angle of 48.1° and a focused laser beam of $\sim 30 \mu\text{m}$. The ISLS system uses a pump-and-probe technique with an infrared pump laser of 1064-nm wavelength and a green probe laser of 532-nm wavelength. Both lasers have pulse widths of 15 ps and repetition rates of 200,000 Hz. The pump laser is split into two excitation beams, which are then recombined at the sample position with a crossing angle of 20.3° . The focused probe laser has a beam size of 30-40 μm . To avoid potential geometrical errors, both BLS and ISLS systems were aligned precisely using a series of reference spots and iris diaphragms, and were calibrated monthly using distilled water and standard glass²⁶. To avoid potential sample degradation due to the metastability of bridgmanite at low pressures, we intentionally started BLS and ISLS measurements from $\sim 24 \text{ GPa}$. BLS and ISLS spectra were collected on two loaded samples in identical orientations as a function of azimuthal angles over 200° with a 10° -step rotation at each experimental pressure. Collected BLS spectra were used to derive V_s , and time-domain ISLS spectra were Fourier-transformed into frequency-domain power spectra to derive V_P of the sample at high pressure (Fig. 1c-e).

To confirm the crystal quality of loaded platelets with neon pressure medium, we performed synchrotron single-crystal XRD at 13 ID-D of GSECARS at APS, ANL at several high-pressure points. Supplementary Fig. 1 shows representative XRD results of the platelet with an orientation of $(-0.50, 0.05, -0.86)$ at ~ 76 GPa. These circular and round diffraction peaks with average FWHM of $\sim 0.04^\circ$ - 0.07° confirmed the high-quality of our crystals in DACs. Analyses of XRD also show consistent orientation information as determined at ambient conditions with small deviations ($<0.2^\circ$).

A complimentary XRD run was conducted on single-crystal Fe₁₀-Al₁₄-Bgm up to 75 GPa at 300 K to evaluate its pressure-volume (P-V) relationship at 13 ID-D of GSECARS at APS, ANL (Supplementary Table 1). Following a literature procedure²⁶, a piece of Fe₁₀-Al₁₄-Bgm platelet, ~ 20 μm in length and ~ 8 μm in thickness, was loaded into a symmetric DAC with 200- μm culets, together with Au as the pressure calibrant and neon as the pressure medium.

Heat capacity on ferropericlase and bridgmanite. Specific heat capacity measurements were performed on polycrystalline bridgmanite²⁶ $\text{Mg}_{0.96}\text{Fe}^{2+}_{0.036}\text{Fe}^{3+}_{0.014}\text{Si}_{0.99}\text{O}_3$ and ferropericlase ($\text{Mg}_{0.8}\text{Fe}_{0.2}$)O using the two- τ relaxation method with a physical property measurement system (PPMS) (Quantum Design) at the Walker Department of Mechanical Engineering at The University of Texas at Austin. Both samples were double-side polished to a dimension of approximately $1\text{ mm} \times 1\text{ mm} \times 0.5\text{ mm}$ for C_P measurements. Liquid helium was used to cool these samples to as low as 2 K (Fig. 1f-g and Supplementary Table 2).

Data analyses on single-crystal C_{ij} of Fe₁₀-Al₁₄-Bgm. Christoffel's equations³⁴ were used to fit collected sound velocities of two single-crystal Fe₁₀-Al₁₄-Bgm platelets as a function of azimuthal angles and to derive its full elastic tensor (Supplementary Fig. 2 and Supplementary Table 3):

$$|C_{ijkl}n_in_j - \rho v^2 \delta_{ik}| = 0 \quad (1)$$

where C_{ijkl} is the elastic tensor with full suffix notation, contracted to C_{ij} in Voigt form in this study, v are measured velocities of V_P , V_{S1} , and V_{S2} , n_i are wave vector direction cosines, and δ_{ik} is the Kronecker delta. We further used a finite-strain theory from the literature²⁹ to fit high-pressure C_{ij} to quantitatively derive their pressure derivatives (Supplementary Fig. 3 and Supplementary Table 4):

$$C_{ij} = (1 + 2f)^{5/2}(C_{ij0} + a_1f + a_1f^2) \quad (2)$$

$$a_1 = (3K_{S0}C'_{ij0} - 5C_{ij0}) \quad (3)$$

$$a_2 = 6K_{S0}C'_{ij} - 14C_{ij0} - 1.5K_{S0}\Delta(3K'_{S0} - 16) \quad (4)$$

where C'_{ij0} and K'_{S0} are pressure derivatives of ambient single-crystal elastic moduli, C_{ij0} , and adiabatic bulk modulus, K_{S0} , respectively, Δ is a constant parameter calculated as: $\Delta = -\delta_{ij}\delta_{kl} - \delta_{il}\delta_{jk} - \delta_{jl}\delta_{ik}$, with values of -3 for C_{11} , C_{22} , C_{33} , and of -1 for C_{44} , C_{55} , C_{66} , C_{12} , C_{13} , C_{23} , and f is the Eulerian strain expressed as:

$$f = \frac{1}{2} \left[(V_0/V)^{2/3} - 1 \right] \quad (5)$$

where V_0 (V) is the unit cell volume at ambient conditions (high-pressure) from XRD. For the principle longitudinal moduli, C_{33} has a greater pressure derivative than those of C_{11} and C_{22} , that results in $C_{33} > C_{22}$ at pressures above ~70 GPa. On the other hand, the pressure derivatives of shear moduli exhibit $C_{44} > C_{66} > C_{55}$. With pressure increasing, the smallest shear moduli at ambient conditions, C_{44} , exceeds C_{55} at pressures above 30 GPa and is expected to be greater than C_{66} at the lowermost mantle pressure. While the off-diagonal moduli display $C_{23} > C_{13} > C_{12}$ at all the pressure ranges with the same trend for their pressure derivatives. We note that the slight difference on pressure derivatives of C_{ij} between this study and *ab initio* calculations for MgSiO₃

bridgmanite³⁸⁻⁴⁰ might come from compositional differences and/or limitations of theoretical simulations.

To further calculate aggregate adiabatic bulk and shear moduli (K_S, μ) of single-crystal Fe10-Al14-Bgm, we employed the Voigt-Reuss-Hill averaging scheme⁵⁷:

$$K_V = (C_{11} + C_{22} + C_{33} + 2(C_{12} + C_{13} + C_{23}))/9 \quad (6)$$

$$K_R = D/E \quad (7)$$

$$K_S = (K_V + K_R)/2 \quad (8)$$

$$\mu_V = (C_{11} + C_{22} + C_{33} + 3(C_{44} + C_{55} + C_{66}) - (C_{12} + C_{13} + C_{23}))/15 \quad (9)$$

$$\mu_R = 15/\left(\frac{4F}{D} + 3\left(\frac{1}{C_{44}} + \frac{1}{C_{55}} + \frac{1}{C_{66}}\right)\right) \quad (10)$$

$$\mu = (\mu_V + \mu_R)/2 \quad (11)$$

where K_V (μ_V) and K_R (μ_R) are upper Voigt and lower Reuss bounds of K_S (μ), respectively, and D , E , and F are three constants, calculated as:

$$D = C_{13}(C_{12}C_{23} - C_{13}C_{22}) + C_{23}(C_{12}C_{13} - C_{11}C_{23}) + C_{33}(C_{11}C_{22} - C_{12}C_{12}) \quad (12)$$

$$E = C_{11}(C_{22} + C_{33} - 2C_{23}) + C_{22}(C_{33} - 2C_{13}) - 2C_{12}C_{33} + C_{12}(2C_{23} - C_{12}) \\ + C_{13}(2C_{12} - C_{13}) + C_{23}(2C_{13} - C_{23}) \quad (13)$$

$$F = C_{11}(C_{22} + C_{33} + C_{23}) + C_{22}(C_{33} + C_{13}) + C_{12}C_{33} - C_{12}(C_{23} + C_{12}) \\ - C_{13}(C_{12} + C_{13}) - C_{23}(C_{13} + C_{23}) \quad (14)$$

Accordingly, aggregate V_P and V_S of single-crystal Fe10-Al14-Bgm can be calculated using:

$$V_P = \sqrt{(K_S + 4\mu/3)/\rho} \quad (15)$$

$$V_S = \sqrt{\mu/\rho} \quad (16)$$

Compared with literature reports on aggregate elastic properties of polycrystalline and single-crystal (Al,Fe)-bearing bridgmanite^{16,17,20,35,38,45,47}, our K_S , μ , V_P , and V_S show a general consistency to the first order (Fig. 2a). In contrast, theoretical calculations on $\text{Mg}_{0.9}\text{Fe}_{0.1}\text{Al}_{0.1}\text{Si}_{0.9}\text{O}_3$ bridgmantite⁵⁸ shows a much lower V_S than those experimental results, indicating an insufficiency of *ab initio* calculations when Fe and Al are incorporated into bridgmanite. This might be due to the complexity of spin and valance states of Fe ions as well as the complicated site occupancies of Fe and Al in the structure of bridgmanite.

High-pressure aggregate K_S and μ of single-crystal Fe10-Al14-Bgm can be fit using third-order Eulerian finite-strain equations²⁹:

$$K_S = (1 + 2f)^{5/2} [K_{S0} + (3K_{S0}K'_{S0} - 5K_{S0})f + 13.5(K_{S0}K'_{S0} - 4K_{S0})f^2] \quad (17)$$

$$\mu = (1 + 2f)^{5/2} [\mu_0 + (3K_{S0}\mu'_0 - 5\mu_0)f + (6K_{S0}\mu'_0 - 24K_{S0} - 14\mu_0 + 4.5K_{S0}K'_{S0})f^2] \quad (18)$$

where K_{S0} (μ_0) is the adiabatic bulk (shear) modulus at ambient conditions, K'_{S0} (μ'_0) is the pressure derivative of K_{S0} (μ_0). The best fits yield $K'_{S0} = 3.50 (\pm 0.04) \text{ GPa}$, $\mu'_0 = 1.87 (\pm 0.02)$, $K_{S0} = 245.8 (\pm 1.7) \text{ GPa}$, and $\mu_0 = 170.0 (\pm 1.5) \text{ GPa}$. We note that literature^{16,45,47} commonly neglect the term at f^2 order when evaluating high-pressure elasticity of bridgmanite. Such approximations are acceptable at relatively low pressures (<40 GPa), where the term f^2 is small and neglectable. However, Helmholtz free energy at higher orders increases with pressure and cannot be simply truncated at high P-T conditions²⁹. Thus, equations used here are more applicable to candidate lower-mantle minerals.

Collected high-pressure XRD patterns of single-crystal Fe10-Al14-Bgm were analyzed to determine its unit cell parameters and volume. We fit P-V at 300 K using third-order Birch-Murnaghan EoS⁵⁹:

$$P = \frac{3}{2} K_{T0} \left[(V_0/V)^{\frac{7}{3}} - (V_0/V)^{\frac{5}{3}} \right] \left\{ 1 + \frac{3}{4} (K'_{T0} - 4) \left[(V_0/V)^{\frac{2}{3}} - 1 \right] \right\} \quad (19)$$

where K_{T0} (V_0) is the isothermal bulk modulus (unit cell volume) at ambient conditions, and K'_{T0} is the pressure derivative of K_{T0} . The best fits show $K_{T0} = 256 (\pm 2) \text{ GPa}$, $K'_{T0} = 4$ (fixed), or $K_{T0} = 259 (\pm 4) \text{ GPa}$, $K'_{T0} = 3.8 (\pm 0.2)$, with fixed V_0 as 163.75 \AA^3 , consistent with early studies^{60,61} on (Al,Fe)-bearing bridgmanite within uncertainties (Supplementary Table 5).

Fe and Al effects on the density and velocity of bridgmanite. Here we assume a linear effect of coupled Fe and Al substitution as well as a total Fe effect of both Fe^{2+} and Fe^{3+} on ρ , K_S , and μ of bridgmanite. Literature density data for bridgmanite with different compositions^{60,61} were fit together using Birch-Murnaghan EoS with fixed $K'_{T0} = 4$ (Supplementary Fig. 4), yielding:

$$\rho_0(\text{Fe}, \text{Al}) = 4.11 + 1.0\text{Fe}_{Bgm} + 0.04\text{Al}_{Bgm} \quad (20)$$

$$K_{T0}(\text{Fe}, \text{Al}) = 258 - 28\text{Fe}_{Bgm} + 101\text{Al}_{Bgm} \quad (21)$$

where Fe_{Bgm} and Al_{Bgm} are Fe and Al contents in bridgmanite, calculated as $\text{Fe}_{Bgm} = \text{Fe}/(\text{Fe} + \text{Mg})$ and $\text{Al}_{Bgm} = \text{Al}/(\text{Al} + \text{Si})$, respectively. The modeled ρ_0 and K_{T0} for end member MgSiO_3 bridgmanite are consistent with literature reports^{45,61} and the effect of Fe on K_{T0} is less significant than that of Al. On the other hand, the best fits to K_S and μ data of bridgmanite^{16,17,45-47} yield:

$$K_{S0}(\text{Fe}, \text{Al}) = 253 - 119\text{Fe}_{Bgm} + 64\text{Al}_{Bgm} \quad (22)$$

$$K'_{S0}(\text{Fe}, \text{Al}) = 4.29 + 0.9\text{Fe}_{Bgm} - 6.05\text{Al}_{Bgm} \quad (23)$$

$$\mu_0(\text{Fe}, \text{Al}) = 174.7 - 4.29\text{Fe}_{Bgm} - 98.9\text{Al}_{Bgm} \quad (24)$$

$$\mu'_0(\text{Fe}, \text{Al}) = 1.67 + 1.10\text{Fe}_{Bgm} + 1.24\text{Al}_{Bgm} \quad (25)$$

We note that 68% residues of K_S , μ , and ρ in the best fits are less than 1.1%, 1.0%, and 0.3%, respectively (1σ).

Fe partitioning between ferropericlasite and bridgmanite as well as the spin crossover in ferropericlasite. Early studies¹⁰ show that Fe partitioning coefficient between bridgmanite and ferropericlasite (K_D , given by $[Fe^{2+}+Fe^{3+}]_{Bgm}/[Mg^{2+}]_{Bgm}/(Fe^{2+}]_{Fp}/[Mg^{2+}]_{Fp}$) could vary significantly with depth as a result of the spin crossover in ferropericlasite. Using literature K_D in a pyrolitic system¹⁰ for our modeling, Fe content in ferropericlasite would change accordingly in the lower mantle. Here we assume a linear Fe effect on K_s , μ and ρ of high-spin (HS) and low-spin (LS) ferropericlasite and fit the literature data together^{27,62-66}. The best fits to density using Birch-Murnaghan EoS with fixed $K'_{T0} = 4$ show (Supplementary Fig. 5):

$$\rho_{0_HS}(Fe) = 3.58 + 2.40Fe_{Fp}; K_{T0_HS}(Fe) = 159.5 - 11.8Fe_{Fp} \quad (26)$$

$$\rho_{0_LS}(Fe) = 3.58 + 2.83Fe_{Fp}; K_{T0_LS}(Fe) = 153.3 + 40.5Fe_{Fp} \quad (27)$$

where Fe_{Fp} is the Fe content in ferropericlasite, given as $Fe_{Fp}=Fe/(Fe+Mg)$, and subscripts ‘‘HS’’ and ‘‘LS’’ indicate properties of HS and LS ferropericlasite, respectively, with the same denotation for other parameters in the followings. Analyses of literature reports^{27,67} were used for Fe effect on μ of ferropericlasite:

$$\mu_{0_HS}(Fe) = 129 - 81.8Fe_{Fp}; \mu'_{0_HS}(Fe) = 2.32 - 1.97Fe_{Fp} \quad (28)$$

$$\mu_{0_LS}(Fe) = 142 - 81.8Fe_{Fp}; \mu'_{0_LS}(Fe) = 2.23 - 1.97Fe_{Fp} \quad (29)$$

To evaluate the spin crossover effect on K_s , μ , and ρ of ferropericlasite, we followed the literature modeling procedure^{27,66,67} using:

$$V(n) = nV_{LS} + (1 - n)V_{HS} \quad (30)$$

$$\frac{V(n)}{Ks(n)} = n \frac{V_{LS}}{Ks_{LS}} + (1 - n) \frac{V_{HS}}{Ks_{HS}} - (V_{LS} - V_{HS}) \frac{\partial n}{\partial P} \Big|_T \quad (31)$$

$$\frac{V(n)}{\mu(n)} \approx n \frac{V_{\text{LS}}}{\mu_{\text{LS}}} + (1 - n) \frac{V_{\text{HS}}}{\mu_{\text{HS}}} \quad (32)$$

where n is the LS fraction at high P-T. We note that studies⁶⁸ indicate that Fe effect on the onset pressure and width of the spin crossover is negligible for relatively Fe-poor ferropericlasite (<25 mol% Fe), but becomes complex for the Fe-rich (Mg,Fe)O counterpart⁶⁸. Our modeling is thus limited to ferropericlasite containing less than 25 mol% Fe, which is most relevant to the lower-mantle composition.

The fully internally-consistent thermoelastic model. V_P , V_S , ρ , and adiabatic temperature profiles of lower-mantle aggregates can be modeled from K_S , μ , ρ , α , and C_P using a fully internally-consistent thermoelastic model²⁹:

$$P(V, T) = P_{300\text{K}} + \gamma \Delta \mathcal{U}_q / V \quad (33)$$

$$K_S(V, T) = K_T(V, T)(1 + \alpha \gamma T) \quad (34)$$

$$K_T(V, T) = K_{T,300\text{K}} + (\gamma + 1 - q_0) \gamma \Delta \mathcal{U}_q / V - \gamma^2 \Delta(C_V T) / V \quad (35)$$

$$\mu = \mu_{300\text{K}} - \eta_{S0} \Delta \mathcal{U}_q / V \quad (36)$$

$$(\partial T / \partial P)_S = \alpha T / \rho C_P \quad (37)$$

where $P_{300\text{K}}$, $K_{T,300\text{K}}$, and $\mu_{300\text{K}}$ are pressure, isothermal bulk moduli, and shear moduli at 300 K, respectively, that can be calculated using eqs. (17)-(19), q_0 is a volume-independent constant, γ is the Grüneisen parameter, η_{S0} is the shear strain derivative of γ , and $\Delta \mathcal{U}_q$ and $\Delta(C_V T)$ are internal energy and heat differences between 300 K and high temperature, respectively. γ and α can be calculated using equations of $\gamma = \gamma_0 (V/V_0)^{q_0}$ and $\alpha = \frac{1}{V} (\partial V / \partial T)_P$. High P-T \mathcal{U}_q and C_V can be modeled with Debye approximations:

$$\mathcal{U}_q(V, T) = 9nRT \left(\frac{\theta_D}{T}\right)^{-3} \int_0^{\theta_D/T} \frac{x^3}{e^x - 1} dx \quad (38)$$

$$C_V(V, T) = 9nRT \left(\frac{\theta_D}{T}\right)^{-3} \int_0^{\theta_D/T} \frac{x^4 e^x}{(e^x - 1)^2} dx \quad (39)$$

where R is the gas constant, n is the number of atoms in the mineral formula, and θ_D is Debye temperature, expressed as:

$$\theta_D = \theta_0 e^{\left(-\frac{\gamma - \gamma_0}{q_0}\right)} \quad (40)$$

where θ_0 is the ambient Debye temperature. C_P can be derived from C_V with $C_P = (1 + \alpha\gamma T)C_V$.

In this fully internally-consistent thermoelastic model, ten parameters are involved to describe thermoelastic properties of each individual mineral, including F_0 , V_0 , K_0 , K'_0 , μ_0 , μ'_0 , θ_0 , γ_0 , q_0 , and η_{s0} . We neglect the parameter F_0 , as it is only related to phase equilibrium and will involve large uncertainties due to limited experimental constraints. V_0 is ambient unit cell volume from XRD. K'_0 is the pressure derivative of isothermal bulk modulus, K_0 . Here, we set K_0 and K'_0 from velocity measurements, because they provide direct velocity information. We note that our measured velocity data are used to relate the adiabatic bulk modulus, K_S , therefore, proper conversions on K_{S0} and K'_{S0} to K_0 and K'_0 have been made using eq. (34). K_0 and K'_0 here are internally consistent. Similarly, μ'_0 and μ_0 can be derived from velocity results. θ_0 , γ_0 , q_0 , and η_{s0} are four parameters related to high temperature extrapolations (see details for constraining in the followed section).

Constraints on thermoelastic parameters of major mantle minerals. Using the fully internally-consistent thermoelastic model²⁹, literature experimental high P-T data and *ab initio* results^{39,67,69,70} were used to benchmark thermoelastic parameters for mantle minerals, including bridgmanite⁷¹, ferropericlase^{27,62-66}, CaSiO₃ perovskite²⁸, ringwoodite⁷², and majoritic garnet⁷³ (Supplementary Table 6, Supplementary Figs. 4-7 and 11). Taking bridgmanite as an example, θ_0 , γ_0 , q_0 , and η_{s0} were taken by fitting literature thermal EoS data of (Mg_{0.87}Fe_{0.13})SiO₃ bridgmanite⁷¹ up to 130 GPa and 2500 K. A representative test of Mg_{0.9}Fe_{0.1}Si_{0.9}Al_{0.1}O₃ bridgmanite shows that with all the

other parameters fixed, given perturbations of $\pm 20\%$, $\pm 30\%$, $\pm 50\%$, $\pm 40\%$ to θ_0 , q_0 , γ_0 , and η_{SO} , respectively, would cause variations in V_P , V_S , and ρ less than 0.6% (Supplementary Fig. 7). We emphasize that these perturbations allow us to cover their upper and lower bounds in literature reports^{29,39,71}. Furthermore, modeled V_P , V_S , and ρ are comparable to those of MgSiO₃ bridgmanite using *ab initio* calculations³⁹, where deviations might come from compositional difference and/or limitations of theoretical simulations. On the other hand, high P-T elastic data for MgO, Mg_{0.94}Fe_{0.06}O, and Mg_{0.75}Fe_{0.25}O ferropericlase^{63,66,74} were used to evaluate values and uncertainties of θ_0 , γ_0 , and q_0 (Supplementary Fig. 5). Our modeled results are consistent with *ab initio* calculations on Mg_{0.8126}Fe_{0.1875}O ferropericlase⁶⁷. As to CaSiO₃ perovskite, we modeled its high P-T elastic data from Gréaux et al.²⁸ and Sun et al.⁷⁵, but excluded those from Thomson et al.⁷⁶ (Supplementary Fig. 6). The density profile by Gréaux et al.²⁸ is consistent with that by Sun et al.⁷⁵, while Thomson et al.⁷⁶ reported much lower density than these studies^{28,75}. Our modelled profiles for CaSiO₃ perovskite fall into the range of theoretical calculations^{69,70}.

Modeling lower-mantle mineralogy and geotherm. Using the aforementioned thermoelastic theory, we model V_P , V_S , and ρ of candidate lower-mantle minerals along an adiabatic geotherm, and compare them with 1D seismic profiles^{1,2}. Due to the iterative process between compositional and thermal parameters, we use 1920(± 40) K as the starting anchor potential temperature at the topmost lower mantle according to literature post-spinel transformation experiments⁷. We note that majoritic garnet gradually transforms into bridgmanite at 1873-2273 K over a wide range at 660-km depth⁷⁷. The total volume percentage of bridgmanite (V_{Bgm}), ferropericlase (V_{Fp}), and CaSiO₃ perovskite (V_{CaPv}) is defined as 100%. Within the framework of a chemically-homogenous adiabatic lower mantle, we assume: (1) V_{Bgm} , V_{Fp} , and V_{CaPv} are constant with depth; (2) Total Fe content (Fe) is constant with depth: $Fe = Fe_{Bgm}V_{Bgm} + Fe_{Fp}V_{Fp}$. Bulk properties of mineral

aggregates are calculated using Voigt-Reuss-Hill averages⁴¹. With all these factors considered, modeled V_P , V_S , and ρ are compared to PREM¹ at 28-130 GPa through minimizing misfits. We neglect topmost and lowermost lower-mantle regions, where the breakdown of majoritic garnet and large temperature gradients as well as transformation of bridgmanite into post-perovskite can significantly affect seismic profiles.

Error propagations on modeled lower-mantle velocity and density profiles. Uncertainties (u) of modeled V_P , V_S , and ρ for lower-mantle aggregates along an adiabatic geotherm in this study would primarily come from three parts: uncertainty of experimental data (u_1), uncertainty in evaluations of the Fe/Al effects on the elasticity bridgmanite and ferropericlae (u_2), and uncertainty in high P-T extrapolations (u_3). u can be calculated as $u = \sqrt{u_1^2 + u_2^2 + u_3^2}$ using standard error propagations. Based on our early discussions on u_1 , u_2 , and u_3 , our modeled high P-T V_P , V_S , and ρ profiles would have typical uncertainties of $\pm 2.2\%$, $\pm 1.8\%$, and $\pm 1.1\%$.

Velocity corrections from high-frequency experimental data to low-frequency seismic profiles. Velocity measurements using BLS and ISLS are performed at high-frequency (GHz) conditions, while seismic profiles typically have frequencies on the order of \sim Hz. Literature⁴⁸ indicate that as a result of the frequency dependence of seismic attenuation, the attenuation factor, q , with frequency, ω , can be represented as:

$$q = \frac{-\Delta E}{2\pi E_{max}} = q_{00}(\omega_{00}/\omega)^\tau \quad (41)$$

where $\Delta E/E_{max}$ is the fraction of internal energy lost in one cycle of seismic waves, q_{00} is the reference factor with frequency ω_{00} , and τ is a model-dependent and frequency-dependent parameter. Velocity variations⁴⁸ between $V_1(\omega_1)$ and $V_2(\omega_2)$ with frequencies of ω_1 and ω_2 , respectively, can be expressed as:

$$\frac{V_2(\omega_2)}{V_1(\omega_1)} = 1 + \frac{q(\omega_1)}{2} \cot\left(\frac{\alpha\pi}{2}\right) \left[1 - \left(\frac{\omega_1}{\omega_2}\right)^\tau\right] \quad (42)$$

Early studies⁷⁸ show that τ generally ranges from 0.2 to 0.4. With τ as ~ 0.3 , velocity differences with frequencies between GHz and Hz are less than 0.3% (Supplementary Fig. 8). We note that this equation is typically applied to anelastic dispersion within seismic frequency, ranging from Hz to several thousands of Hz. This equation is used for correcting frequency-dependent velocity to the first order.

Viscosity of the lower mantle. The viscosity of bridgmanite (10^{21} - 10^{23} Pa·s) was inferred to be much higher than that of ferropericlase (10^{18} - 10^{20} Pa·s)⁵⁴. Compared with a “load bearing framework” (LBF) model to calculate the viscosity of multiple-phase aggregates with equally-portioned strains between grains, literature results indicate that a non-linear “inter-connected weak layers” (IWL) model⁷⁹ is more applicable for the lower mantle containing rheologically weak and strong grains. The bulk lower-mantle viscosity (η) can be calculated as a function of ferropericlase volume fraction (x_{Fp}):

$$\eta = \frac{[a^2 - 2a(a-1)x_{Fp} + (a-1)^2x_{Fp}^2]b}{a^2 + (b-a^2)x_{Fp}} \eta_{Fp} \quad (43)$$

where a and b are density and viscosity contrasts between bridgmanite (ρ_{Bgm} , η_{Bgm}) and ferropericlase (ρ_{Fp} , η_{Fp}), calculated as $a = \rho_{Bgm}/\rho_{Fp}$ and $b = \eta_{Bgm}/\eta_{Fp}$, respectively. We neglect the role of CaSiO_3 perovskite due to the lack of reliable viscosity from the literature.

References:

- 1 Dziewonski, A. M. & Anderson, D. L. Preliminary Reference Earth Model. *Phys Earth Planet In* **25**, 297-356, doi:Doi 10.1016/0031-9201(81)90046-7 (1981).
- 2 Kennett, B. L. N., Engdahl, E. R. & Buland, R. Constraints on Seismic Velocities in the Earth from Travel-Times. *Geophys J Int* **122**, 108-124, doi:DOI 10.1111/j.1365-246X.1995.tb03540.x (1995).
- 3 Shearer, P. M. & Flanagan, M. P. Seismic velocity and density jumps across the 410-and 660-kilometer discontinuities. *Science* **285**, 1545-1548 (1999).
- 4 Estabrook, C. H. & Kind, R. The nature of the 660-kilometer upper-mantle seismic discontinuity from precursors to the PP phase. *Science* **274**, 1179-1182 (1996).
- 5 Castle, J. C. & Creager, K. C. Local sharpness and shear wave speed jump across the 660-km discontinuity. *Journal of Geophysical Research: Solid Earth* **105**, 6191-6200, doi:10.1029/1999jb900424 (2000).
- 6 Lawrence, J. F. & Shearer, P. M. Constraining seismic velocity and density for the mantle transition zone with reflected and transmitted waveforms. *Geochemistry, Geophysics, Geosystems* **7** (2006).
- 7 Stacey, F. & Davis, P. (Cambridge Univ. Press, 2008).
- 8 Ringwood, A. E. *Composition and petrology of the earth's mantle [by] AE Ringwood.* (1975).
- 9 Anderson, D. L. & Bass, J. D. Mineralogy and composition of the upper mantle. *Geophys Res Lett* **11**, 637-640 (1984).
- 10 Irifune, T. *et al.* Iron partitioning and density changes of pyrolite in Earth's lower mantle. *Science* **327**, 193-195 (2010).
- 11 Weidner, D. J. & Wang, Y. Chemical - and Clapeyron - induced buoyancy at the 660 km discontinuity. *Journal of Geophysical Research: Solid Earth* **103**, 7431-7441 (1998).
- 12 Wu, W., Ni, S. & Irving, J. C. Inferring Earth's discontinuous chemical layering from the 660-kilometer boundary topography. *Science* **363**, 736-740 (2019).
- 13 McDonough, W. F. & Sun, S.-S. The composition of the Earth. *Chem Geol* **120**, 223-253 (1995).
- 14 Allègre, C. J., Poirier, J.-P., Humler, E. & Hofmann, A. W. The chemical composition of the Earth. *Earth Planet Sc Lett* **134**, 515-526 (1995).
- 15 Hofmann, A. W. Mantle geochemistry: the message from oceanic volcanism. *Nature* **385**, 219 (1997).
- 16 Kurnosov, A., Marquardt, H., Frost, D., Ballaran, T. B. & Ziberna, L. Evidence for a Fe³⁺-rich pyrolitic lower mantle from (Al, Fe)-bearing bridgmanite elasticity data. *Nature* **543**, 543-546 (2017).
- 17 Murakami, M., Ohishi, Y., Hirao, N. & Hirose, K. A perovskitic lower mantle inferred from high-pressure, high-temperature sound velocity data. *Nature* **485**, 90-94, doi:10.1038/nature11004 (2012).
- 18 Mashino, I., Murakami, M., Miyajima, N. & Petitgirard, S. J. P. o. t. N. A. o. S. Experimental evidence for silica-enriched Earth's lower mantle with ferrous iron dominant bridgmanite. *Proceedings of the National Academy of Sciences* (2020).
- 19 Cottaar, S., Heister, T., Rose, I. & Unterborn, C. BurnMan: A lower mantle mineral physics toolkit. *Geochemistry, Geophysics, Geosystems* **15**, 1164-1179 (2014).
- 20 Lin, J.-F., Mao, Z., Yang, J. & Fu, S. Elasticity of lower-mantle bridgmanite. *Nature* **564**, E18-E26, doi:10.1038/s41586-018-0741-7 (2018).
- 21 Anderson, O. The Earth's core and the phase diagram of iron. *Philosophical Transactions of the Royal Society of London A: Mathematical, Physical and Engineering Sciences* **306**, 21-35 (1982).
- 22 Katsura, T., Yoneda, A., Yamazaki, D., Yoshino, T. & Ito, E. Adiabatic temperature profile in the mantle. *Phys Earth Planet In* **183**, 212-218, doi:10.1016/j.pepi.2010.07.001 (2010).

- 23 Brown, J. & Shankland, T. Thermodynamic parameters in the Earth as determined from seismic profiles. *Geophys J Int* **66**, 579-596 (1981).
- 24 Valencia-Cardona, J. J. *et al.* Influence of the iron spin crossover in ferropericlase on the lower mantle geotherm. *Geophys Res Lett* **44**, 4863-4871, doi:10.1002/2017gl073294 (2017).
- 25 Fu, S. *et al.* Water concentration in single - crystal (Al, Fe) - bearing bridgmanite grown from the hydrous melt: implications for dehydration melting at the topmost lower mantle. *Geophys Res Lett* (2019).
- 26 Fu, S. *et al.* Abnormal Elasticity of Fe - Bearing Bridgmanite in the Earth's Lower Mantle. *Geophys Res Lett* **45**, 4725-4732, doi:doi:10.1029/2018GL077764 (2018).
- 27 Yang, J., Tong, X. Y., Lin, J. F., Okuchi, T. & Tomioka, N. Elasticity of Ferropericlase across the Spin Crossover in the Earth's Lower Mantle. *Sci Rep-Uk* **5** (2015).
- 28 Gréaux, S. *et al.* Sound velocity of CaSiO₃ perovskite suggests the presence of basaltic crust in the Earth's lower mantle. *Nature* **565**, 218 (2019).
- 29 Stixrude, L. & Lithgow-Bertelloni, C. Thermodynamics of mantle minerals—I. Physical properties. *Geophys J Int* **162**, 610-632 (2005).
- 30 Akaogi, M. & Ito, E. Heat-Capacity of MgSiO₃ Perovskite. *Geophys Res Lett* **20**, 105-108, doi:Doi 10.1029/92gl02655 (1993).
- 31 Akaogi, M., Kojitani, H., Morita, T., Kawaji, H. & Atake, T. Low-temperature heat capacities, entropies and high-pressure phase relations of MgSiO₃ ilmenite and perovskite. *Phys Chem Miner* **35**, 287-297 (2008).
- 32 Tsuchiya, T. & Wang, X. Ab initio investigation on the high - temperature thermodynamic properties of Fe³⁺ - bearing MgSiO₃ perovskite. *Journal of Geophysical Research: Solid Earth* **118**, 83-91 (2013).
- 33 Fukui, H., Tsuchiya, T. & Baron, A. Q. Lattice dynamics calculations for ferropericlase with internally consistent LDA+ U method. *Journal of Geophysical Research: Solid Earth* **117** (2012).
- 34 Every, A. General closed-form expressions for acoustic waves in elastically anisotropic solids. *Physical Review B* **22**, 1746 (1980).
- 35 Fu, S. *et al.* Single-crystal elasticity of (Al,Fe)-bearing bridgmanite and seismic anisotropy at the topmost lower mantle. *Earth Planet Sc Lett* **518**, 116-126 (2019).
- 36 Fukui, H. *et al.* Effect of cation substitution on bridgmanite elasticity: A key to interpret seismic anomalies in the lower mantle. *Sci Rep-Uk* **6**, 33337 (2016).
- 37 Yeganeh-Haeri, A. Synthesis and re-investigation of the elastic properties of single-crystal magnesium silicate perovskite. *Phys Earth Planet In* **87**, 111-121 (1994).
- 38 Karki, B. *et al.* Elastic properties of orthorhombic MgSiO₃ perovskite at lower mantle pressures. *Am Mineral* **82**, 635-638 (1997).
- 39 Wentzcovitch, R., Karki, B., Cococcioni, M. & De Gironcoli, S. Thermoelastic Properties of MgSiO₃-Perovskite: Insights on the Nature of the Earth's Lower Mantle. *Phys Rev Lett* **92**, 018501 (2004).
- 40 Li, L. *et al.* Elasticity of (Mg,Fe)(Si,Al)O₃-perovskite at high pressure. *Earth Planet Sc Lett* **240**, 529-536 (2005).
- 41 Hill, R. The Elastic Behaviour of a Crystalline Aggregate. *P Phys Soc Lond B* **65**, 349 (1952).
- 42 McCammon, C. Perovskite as a possible sink for ferric iron in the lower mantle. *Nature* **387**, 694 (1997).
- 43 Marquardt, H. *et al.* Elastic shear anisotropy of ferropericlase in Earth's lower mantle. *Science* **324**, 224-226 (2009).
- 44 Williamson, E. D. & Adams, L. H. Density distribution in the Earth. *Journal of the Washington Academy of Sciences* **13**, 413-428 (1923).

- 45 Chantel, J., Frost, D. J., McCammon, C. A., Jing, Z. C. & Wang, Y. B. Acoustic velocities of pure and iron-bearing magnesium silicate perovskite measured to 25 GPa and 1200 K. *Geophys Res Lett* **39**, doi:Artn L19307 10.1029/2012gl053075 (2012).
- 46 Murakami, M., Sinogeikin, S. V., Hellwig, H., Bass, J. D. & Li, J. Sound velocity of MgSiO₃ perovskite to Mbar pressure. *Earth and Planetary Science Letters* **256**, 47-54 (2007).
- 47 Jackson, J. M., Zhang, J., Shu, J., Sinogeikin, S. V. & Bass, J. D. High - pressure sound velocities and elasticity of aluminous MgSiO₃ perovskite to 45 GPa: Implications for lateral heterogeneity in Earth's lower mantle. *Geophys Res Lett* **32** (2005).
- 48 Lekić, V., Matas, J., Panning, M. & Romanowicz, B. Measurement and implications of frequency dependence of attenuation. *Earth Planet Sc Lett* **282**, 285-293 (2009).
- 49 Bunge, H. P., Ricard, Y. & Matas, J. Non - adiabaticity in mantle convection. *Geophys Res Lett* **28**, 879-882 (2001).
- 50 Irifune, T. & Ringwood, A. Phase transformations in a harzburgite composition to 26 GPa: implications for dynamical behaviour of the subducting slab. *Earth Planet Sc Lett* **86**, 365-376 (1987).
- 51 Xu, W., Lithgow-Bertelloni, C., Stixrude, L. & Ritsema, J. The effect of bulk composition and temperature on mantle seismic structure. *Earth Planet Sc Lett* **275**, 70-79 (2008).
- 52 Campbell, I. H. & O'Neill, H. S. C. J. N. Evidence against a chondritic Earth. **483**, 553-558 (2012).
- 53 Goes, S., Agrusta, R., Van Hunen, J. & Garel, F. Subduction-transition zone interaction: A review. *Geosphere* **13**, 644-664 (2017).
- 54 Yamazaki, D. & Karato, S.-i. Some mineral physics constraints on the rheology and geothermal structure of Earth's lower mantle. *Am Mineral* **86**, 385-391 (2001).
- 55 Ballmer, M. D., Houser, C., Hernlund, J. W., Wentzcovitch, R. M. & Hirose, K. Persistence of strong silica-enriched domains in the Earth's lower mantle. *Nat Geosci* **10**, 236-240 (2017).
- 56 Dewaele, A., Loubeyre, P. & Mezouar, M. Equations of state of six metals above 94 GPa. *Phys Rev B* **70**, 094112 (2004).
- 57 Hill, R. The Elastic Behaviour of a Crystalline Aggregate. *P Phys Soc Lond B* **65**, 396-396 (1952).
- 58 Shukla, G., Cococcioni, M. & Wentzcovitch, R. M. Thermoelasticity of Fe³⁺ - and Al - bearing bridgmanite: Effects of iron spin crossover. *Geophys Res Lett* **43**, 5661-5670 (2016).
- 59 Birch, F. Finite Strain Isotherm and Velocities for Single-Crystal and Polycrystalline NaCl at High-Pressures and 300-Degree-K. *J Geophys Res* **83**, 1257-1268, doi:Doi 10.1029/Jb083ib03p01257 (1978).
- 60 Mao, Z. *et al.* Equation of state and hyperfine parameters of high-spin bridgmanite in the Earth's lower mantle by synchrotron X-ray diffraction and Mössbauer spectroscopy. *Am Mineral* **102**, 357-368 (2017).
- 61 Boffa Ballaran, T. *et al.* Effect of chemistry on the compressibility of silicate perovskite in the lower mantle. *Earth Planet Sc Lett* **333**, 181-190, doi:10.1016/j.epsl.2012.03.029 (2012).
- 62 Speziale, S., Zha, C. S., Duffy, T. S., Hemley, R. J. & Mao, H. k. Quasi - hydrostatic compression of magnesium oxide to 52 GPa: Implications for the pressure - volume - temperature equation of state. *Journal of Geophysical Research: Solid Earth* **106**, 515-528 (2001).
- 63 Yang, J. *et al.* Elasticity of ferropervicite and seismic heterogeneity in the Earth's lower mantle. *Journal of Geophysical Research: Solid Earth* (2016).
- 64 Marquardt, H., Speziale, S., Reichmann, H. J., Frost, D. J. & Schilling, F. R. Single-crystal elasticity of (Mg_{0.9}Fe_{0.1})O to 81 GPa. *Earth Planet Sc Lett* **287**, 345-352 (2009).
- 65 Fei, Y. W. *et al.* Spin transition and equations of state of (Mg,Fe)O solid solutions. *Geophys Res Lett* **34**, doi:Artn L17307 (2007).

- 66 Mao, Z., Lin, J. F., Liu, J. & Prakapenka, V. B. Thermal equation of state of lower-mantle ferropericlase across the spin crossover. *Geophys Res Lett* **38**, doi:Artn L23308 (2011).
- 67 Wu, Z. Q., Justo, J. F. & Wentzcovitch, R. M. Elastic Anomalies in a Spin-Crossover System: Ferropericlase at Lower Mantle Conditions. *Phys Rev Lett* **110**, doi:Artn 228501 (2013).
- 68 Speziale, S. *et al.* Effects of Fe spin transition on the elasticity of (Mg,Fe)O magnesiowustites and implications for the seismological properties of the Earth's lower mantle. *J Geophys Res-Sol Ea* **112**, doi:Artn B10212 (2007).
- 69 Kawai, K. & Tsuchiya, T. Small shear modulus of cubic CaSiO₃ perovskite. *Geophys Res Lett* **42**, 2718-2726 (2015).
- 70 Li, L. *et al.* Elasticity of CaSiO₃ perovskite at high pressure and high temperature. *Phys Earth Planet In* **155**, 249-259, doi:10.1016/j.pepi.2005.12.006 (2006).
- 71 Wolf, A. S., Jackson, J. M., Dera, P. & Prakapenka, V. B. The thermal equation of state of (Mg, Fe)SiO₃ bridgmanite (perovskite) and implications for lower mantle structures. *J Geophys Res-Sol Ea* **120**, 7460-7489, doi:10.1002/2015JB012108 (2015).
- 72 Higo, Y., Inoue, T., Irifune, T., Funakoshi, K.-i. & Li, B. Elastic wave velocities of (Mg_{0.91}Fe_{0.09})₂SiO₄ ringwoodite under P–T conditions of the mantle transition region. *Phys Earth Planet In* **166**, 167-174 (2008).
- 73 Irifune, T. *et al.* Sound velocities of majorite garnet and the composition of the mantle transition region. *Nature* **451**, 814-817 (2008).
- 74 Fan, D. *et al.* Elasticity of single-crystal periclase at high pressure and temperature: The effect of iron on the elasticity and seismic parameters of ferropericlase in the lower mantle. *American Mineralogist: Journal of Earth and Planetary Materials* **104**, 262-275 (2019).
- 75 Sun, N. *et al.* Confirming a pyrolitic lower mantle using self - consistent pressure scales and new constraints on CaSiO₃ perovskite. *Journal of Geophysical Research: Solid Earth* **121**, 4876-4894 (2016).
- 76 Thomson, A. R. *et al.* Seismic velocities of CaSiO₃ perovskite can explain LLSVPs in Earth's lower mantle. *Nature*, doi:10.1038/s41586-019-1483-x (2019).
- 77 Hirose, K., Fei, Y., Ono, S., Yagi, T. & Funakoshi, K.-i. In situ measurements of the phase transition boundary in Mg₃Al₂Si₃O₁₂: implications for the nature of the seismic discontinuities in the Earth's mantle. *Earth Planet Sc Lett* **184**, 567-573 (2001).
- 78 Karato, S.-I. & Spetzler, H. Defect microdynamics in minerals and solid - state mechanisms of seismic wave attenuation and velocity dispersion in the mantle. *Rev Geophys* **28**, 399-421 (1990).
- 79 Takeda, Y.-T. Flow in rocks modelled as multiphase continua: Application to polymineralic rocks. *Journal of Structural Geology* **20**, 1569-1578 (1998).

Figure captions:

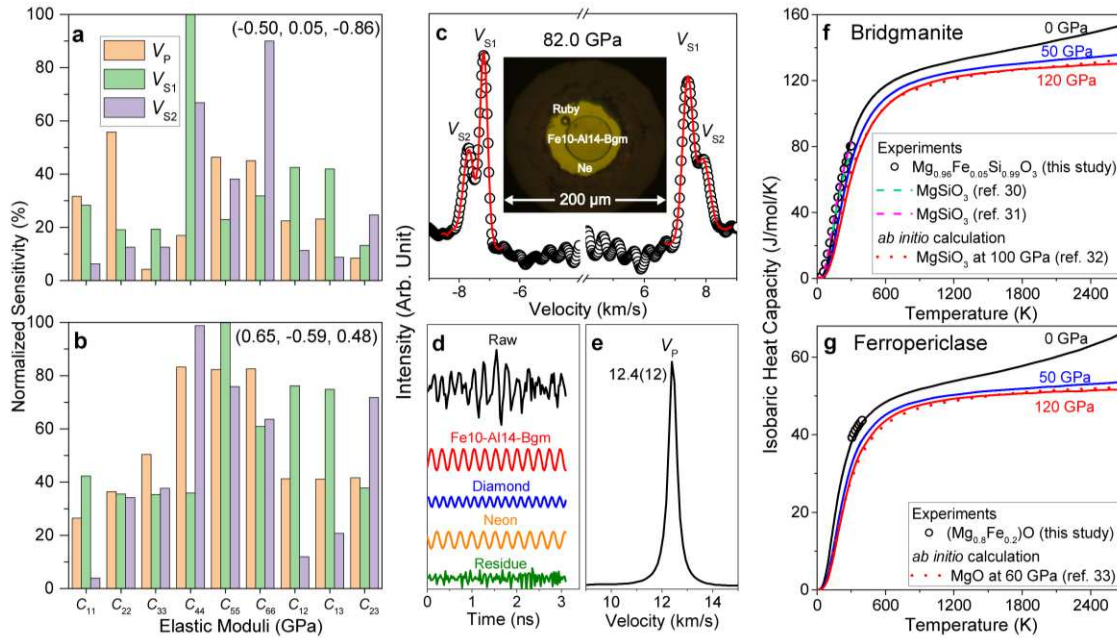


Fig. 1. Selections of single-crystal platelets for sound velocity measurements and heat capacity of bridgmanite and ferropericlasite. **a** and **b**, Sensitivity analyses of C_{ij} to experimentally measured V_P , V_{S1} , and V_{S2} of single-crystal bridgmanite within two crystallographic orientations of $(-0.50, 0.05, -0.86)$ and $(0.65, -0.59, 0.48)$, respectively. The calculation follows a literature³⁵ for an orthorhombic structure with nine C_{ij} . **c-e**, Representative BLS, ISLS, and power spectra of single-crystal Fe10-Al14-Bgm at ~ 82 GPa and 300 K. Open circles are raw BLS data and red lines are best fits to derive V_{S1} and V_{S2} . Collected time-domain ISLS spectra are Fourier-transformed into frequency-domain power spectra to derive V_P . The insert in **c** shows an image of the sample chamber with a Fe10-Al14-Bgm platelet and ruby sphere pressure calibrant. **f** and **g**, High P-T C_P of bridgmanite and ferropericlasite. Open circles are our measured C_P on polycrystalline $\text{Mg}_{0.96}\text{Fe}_{0.05}\text{Si}_{0.99}\text{O}_3$ bridgmanite and $(\text{Mg}_{0.8}\text{Fe}_{0.2})\text{O}$ ferropericlasite at ambient pressure. Dashed green and pink lines are literature measurements on MgSiO_3 bridgmanite^{30,31}. Solid lines are modeled C_P as a function of temperature at ambient pressure (0 GPa, black), 50 GPa (blue), and 120 GPa (red), based on Debye approximations. Dotted red lines are *ab initio* calculations for MgSiO_3 bridgmanite³² and MgO periclasite³³ for comparisons.

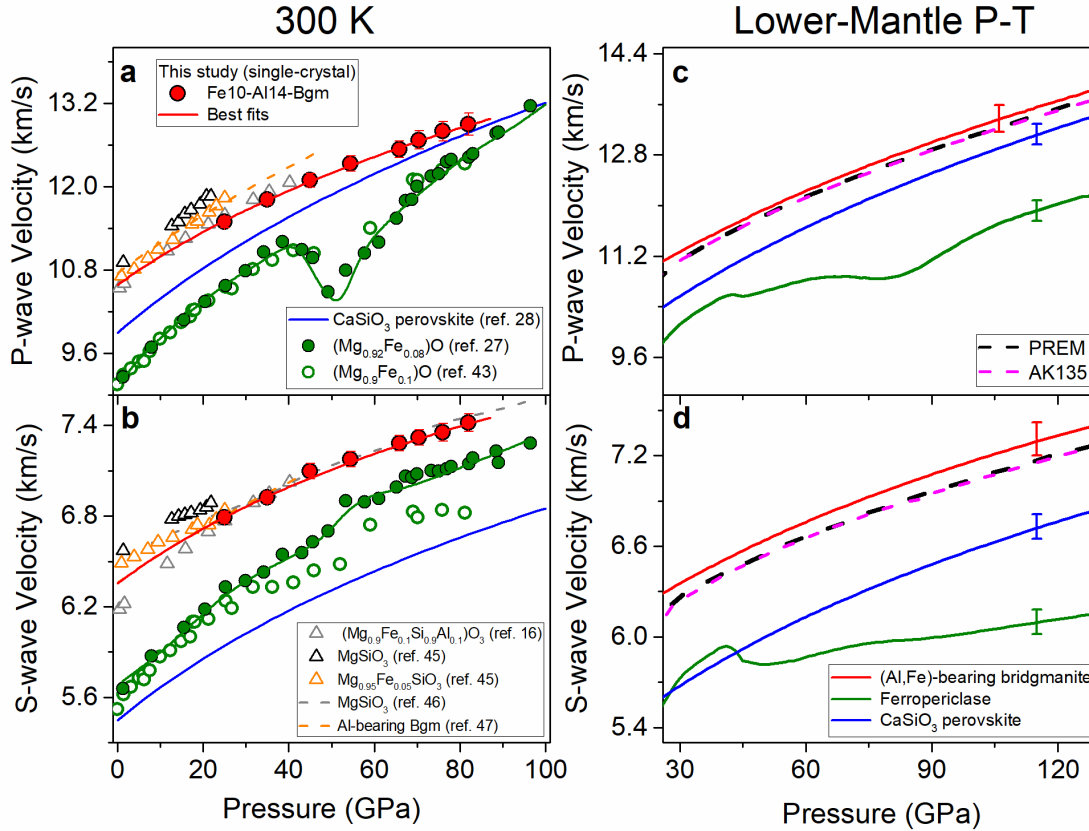


Figure 2 | Velocity profiles of major lower-mantle minerals at high P-T. **a and b**, Aggregate V_P and V_S at high pressure and 300 K. Solid red symbols are aggregate sound velocities of single-crystal Fe10-Al14-Bgm in this study, and solid red lines are the best fits using a finite-strain theory²⁹. Dashed lines and open triangles are literature data for different bridgmanite compositions: $MgSiO_3$ (black triangles)⁴⁵ and $Mg_{0.95}Fe_{0.05}SiO_3$ with $Fe^{3+}/\sum Fe=0.2$ (orange triangles)⁴⁵; $(Mg_{0.9}Fe_{0.1}Si_{0.9}Al_{0.1})O_3$ with $Fe^{3+}/\sum Fe=0.67$ (gray triangle)¹⁶; $MgSiO_3$ (dashed gray lines)⁴⁶ and Al-bearing bridgmanite containing 5.1 wt% Al_2O_3 (dashed orange lines)⁴⁷. Velocity profiles of $CaSiO_3$ perovskite²⁸ (solid blue lines from modeling) and ferropericlase^{27,43} (solid and open olive circles; olive lines show finite-strain fitting) at 300 K are plotted for comparisons. Uncertainties are smaller than symbols when not shown. **c and d**, V_P and V_S along an adiabat geotherm derived in our best-fit model (refer to Fig. 3 and Supplementary Fig. 9). Red lines: (Al,Fe)-bearing bridgmanite; olive lines: ferropericlase; blue lines: $CaSiO_3$ perovskite. K_D between bridgmanite and ferropericlase with depth is taken from the literature¹⁰. The flattening in V_S of ferropericlase above ~ 45 GPa results from Fe preferentially partitioning into ferropericlase across the spin crossover. Seismic profiles^{1,2} are plotted as dashed black and pink lines. Vertical ticks show one standard deviation ($\pm 1\sigma$) derived from error propagations.

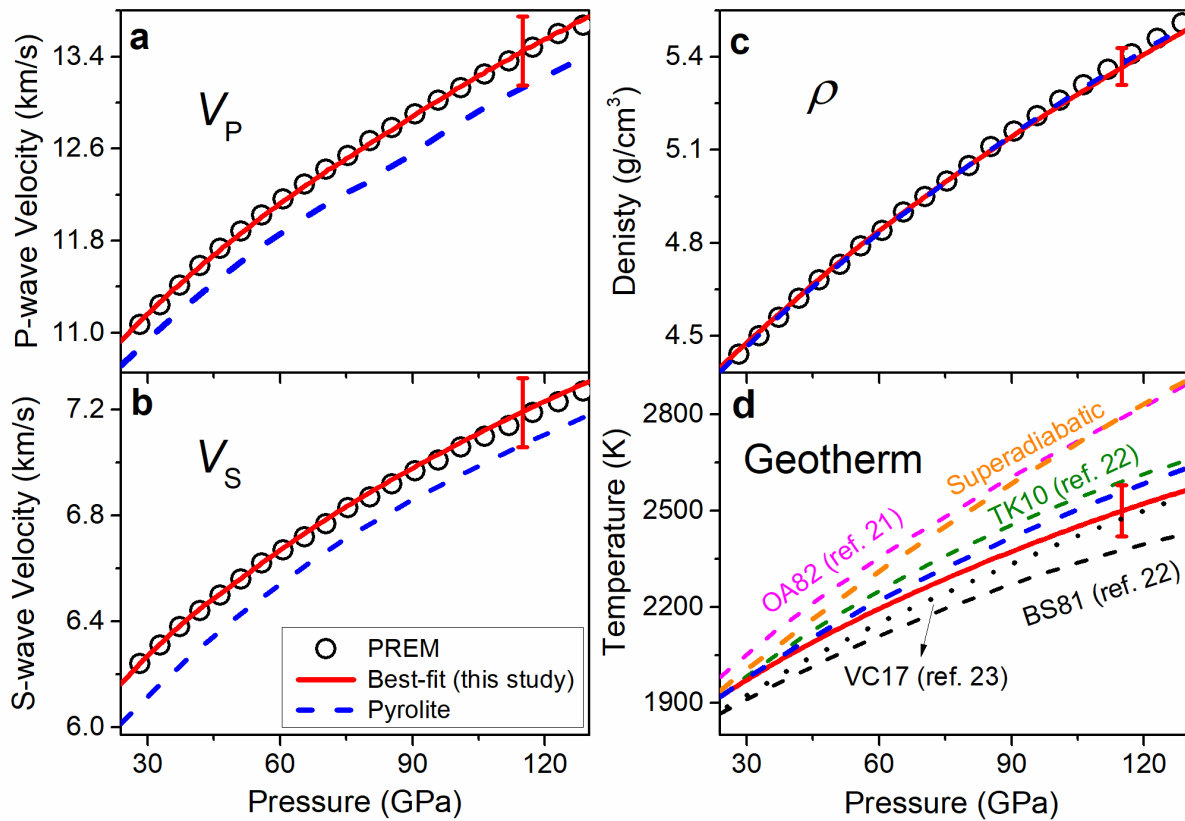


Figure 3 | Modeled velocity, density, and temperature profiles of the lower mantle. a, V_P ; b, V_S ; c, ρ ; d, Geotherm. Solid red lines are our best-fits to PREM (open circles)¹ based on the fully internally-consistent thermoelastic model. Modeled results for a pyrolitic lower mantle¹⁰ are plotted as dashed blue lines. Our best-fit model shows the lower mantle is composed of $\sim 88.7(\pm 2.0)$ vol% bridgmanite, $\sim 4.3(\pm 2.0)$ vol% ferropericlase, and 7 vol% (fixed) CaSiO_3 perovskite. In **d**, solid red line shows the our derived adiabatic geotherm, whereas an adiabat for pyrolite (dashed blue line) and a superadibatic geotherm (dashed orange line) with Bullen's parameter as ~ 0.8 are plotted for comparisons. Dashed olive²² and pink²¹ lines are literature models assuming a pyrolitic-whole-mantle convection and layered-mantle convection, respectively. Dashed black line²³ is an isentropic geotherm using entropies of mantle minerals based on the Debye model. Dotted black line is modeled for a chondritic composition from *ab initio* calculations²⁴. Vertical red ticks represent one standard deviation ($\pm 1\sigma$).

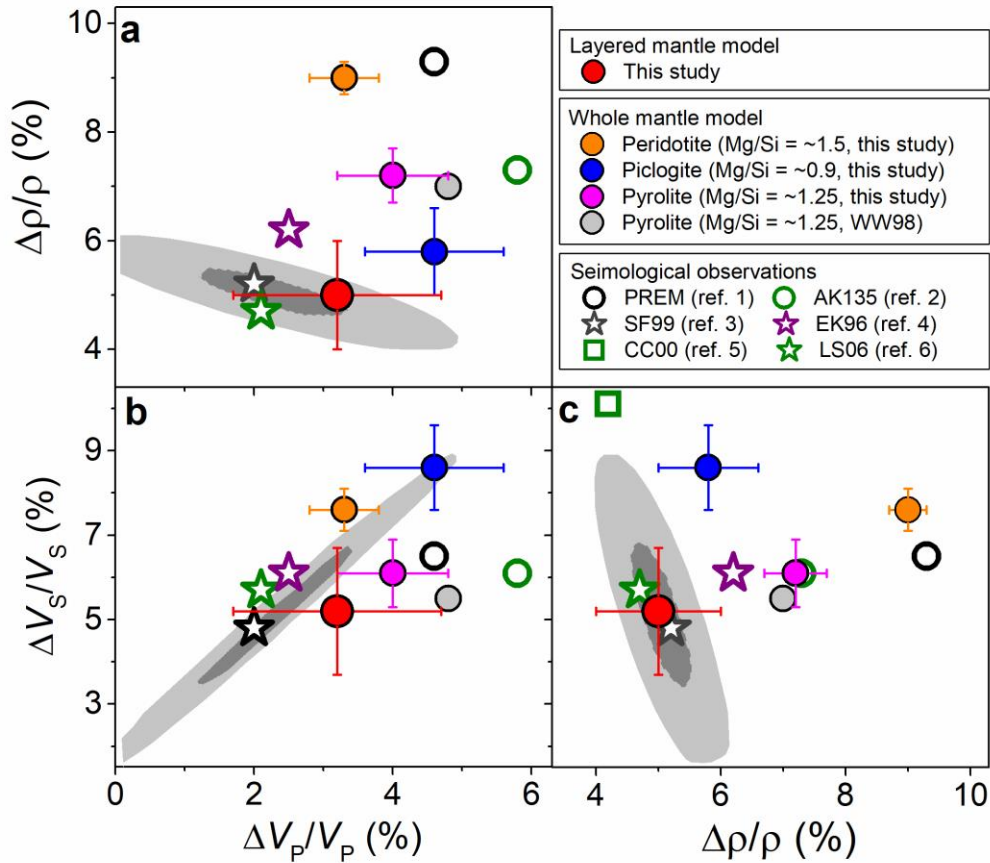


Figure 4 | Comparisons of velocity and density jumps across the 660-km discontinuity between seismic observations and mantle compositional models. a, $\Delta\rho/\rho$ versus $\Delta V_P/V_P$; b, $\Delta V_S/V_S$ versus $\Delta V_P/V_P$; c, $\Delta V_S/V_S$ versus $\Delta\rho/\rho$. Two sets of compositional models are considered here: chemically layered mantle and chemically homogeneous whole mantle. Solid red circles are results for a chemically layered mantle with a pyrolitic transition zone⁸ and bridgmanite-predominant lower mantle in this study. Solid pink, orange, and blue circles are calculations for a chemically homogeneous whole mantle with Mg/Si of ~ 1.5 (peridotite⁵⁰), ~ 1.25 (pyrolite⁸), and ~ 0.9 (piclogite⁹), respectively. Literature results¹¹ for a pyrolitic whole mantle are plotted as solid gray circles (WW98). Open symbols are from seismic observations: EK96 (open purple stars)⁴; LS06 (open olive stars)⁶; CC00 (open olive squares)⁵; SF99 (open black stars)³; PREM (open black circles)¹; AK135 (open olive circles)². Shaded dark and light gray areas are confidence ellipsoids within $\pm 1\sigma$ and $\pm 2\sigma$ limits, respectively, from Shearer and Flanagan³.

Figures

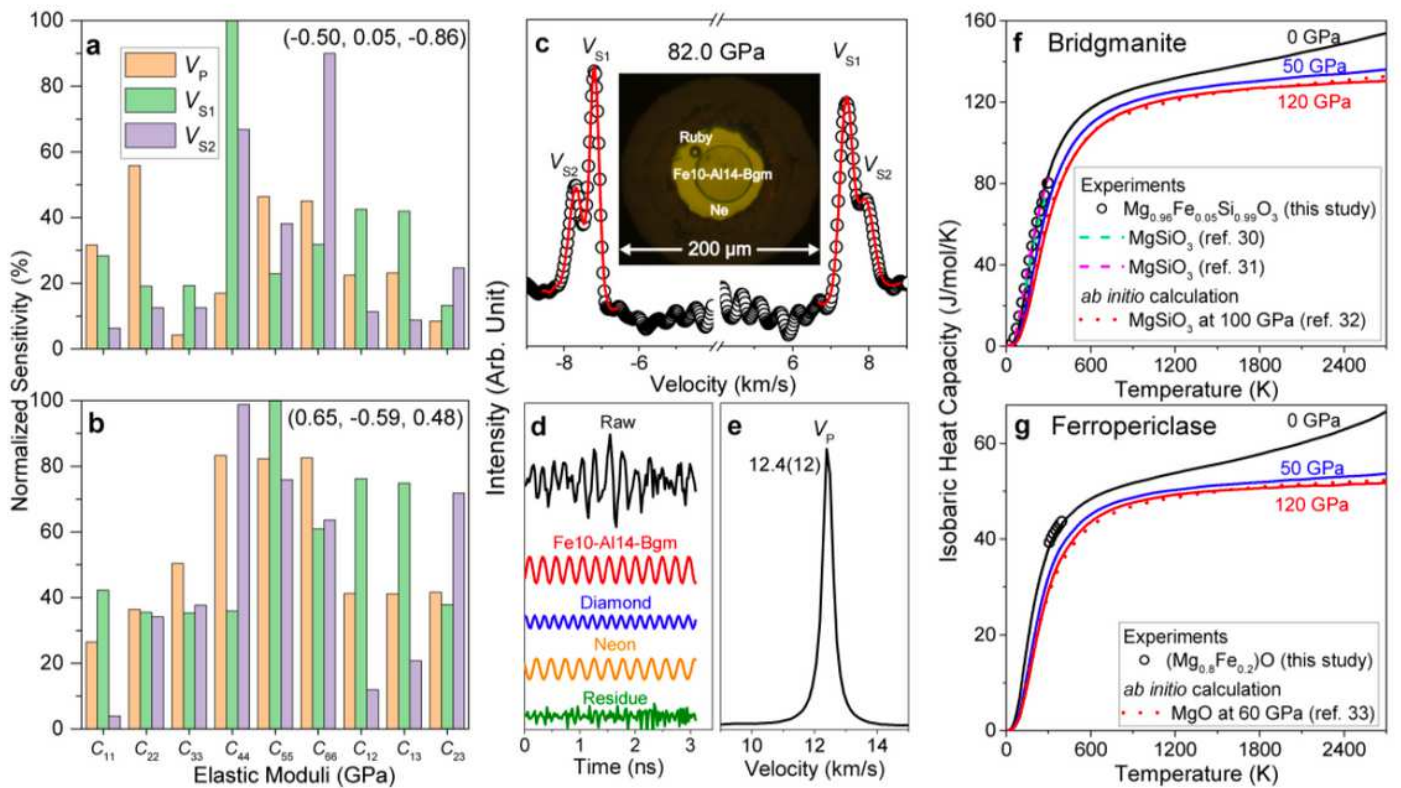


Figure 1

Selections of single-crystal platelets for sound velocity measurements and heat capacity of bridgmanite and ferropericlyase. a and b, Sensitivity analyses of C_{ij} to experimentally measured V_P , V_{S1} , and V_{S2} of single-crystal bridgmanite within two crystallographic orientations of $(-0.50, 0.05, -0.86)$ and $(0.65, -0.59, 0.48)$, respectively. The calculation follows a literature³⁵ for an orthorhombic structure with nine C_{ij} . c-e, Representative BLS, ISLS, and power spectra of single-crystal Fe10-Al14-Bgm at ~ 82 GPa and 300 K. Open circles are raw BLS data and red lines are best fits to derive V_{S1} and V_{S2} . Collected time-domain ISLS spectra are Fourier-transformed into frequency-domain power spectra to derive V_P . The insert in c shows an image of the sample chamber with a Fe10-Al14-Bgm platelet and ruby sphere pressure calibrant. f and g, High P-T CP of bridgmanite and ferropericlyase. Open circles are our measured CP on polycrystalline $Mg_{0.96}Fe_{0.05}Si_{0.99}O_3$ bridgmanite and $(Mg_{0.8}Fe_{0.2})O$ ferropericlyase at ambient pressure. Dashed green and pink lines are literature measurements on $MgSiO_3$ bridgmanite^{30,31}. Solid lines are modeled CP as a function of temperature at ambient pressure (0 GPa, black), 50 GPa (blue), and 120 GPa (red), based on Debye approximations. Dotted red lines are ab initio calculations for $MgSiO_3$ bridgmanite³² and MgO periclyase³³ for comparisons.

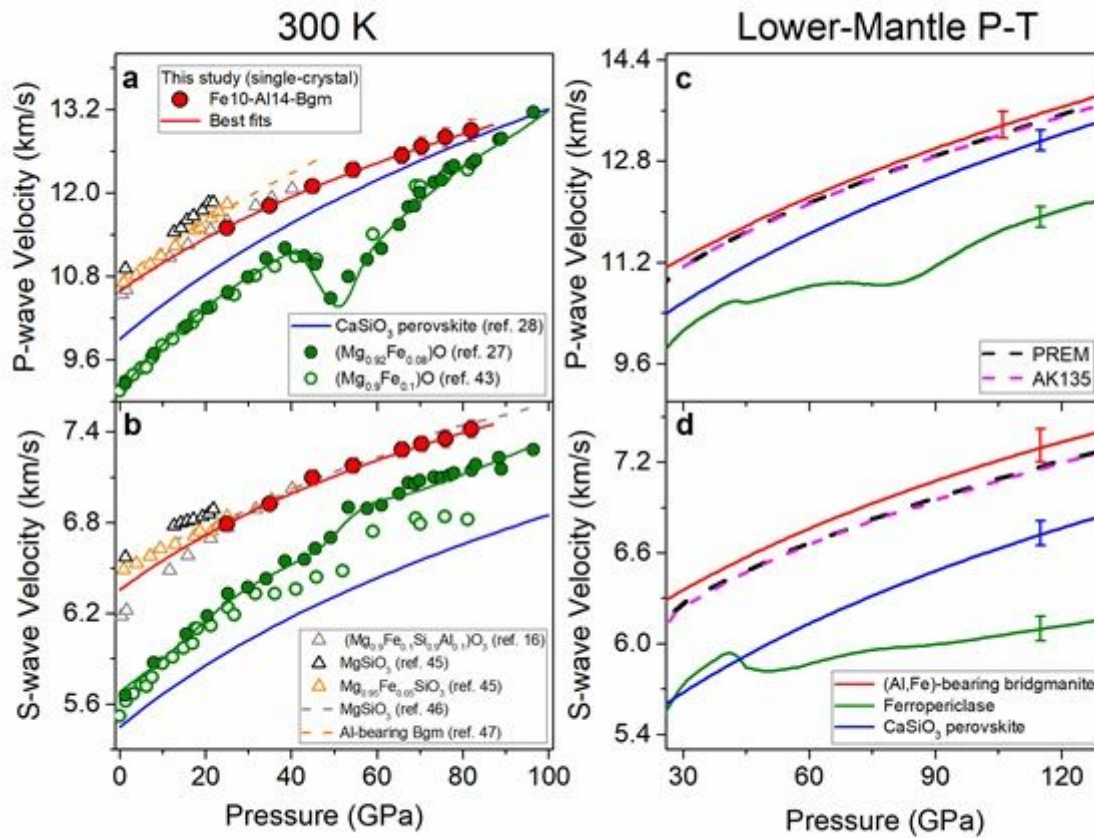


Figure 2

Velocity profiles of major lower-mantle minerals at high P-T. a and b, Aggregate VP and VS at high pressure and 300 K. Solid red symbols are aggregate sound velocities of single-crystal Fe10-Al14-Bgm in this study, and solid red lines are the best fits using a finite-strain theory²⁹. Dashed lines and open triangles are literature data for different bridgmanite compositions: MgSiO₃ (black triangles)⁴⁵ and Mg_{0.95}Fe_{0.05}SiO₃ with Fe³⁺/ΣFe=0.2 (orange triangles)⁴⁵; (Mg_{0.9}Fe_{0.1}Si_{0.9}Al_{0.1})O₃ with Fe³⁺/ΣFe=0.67 (gray triangle)¹⁶; MgSiO₃ (dashed gray lines)⁴⁶ and Al-bearing bridgmanite containing 5.1 wt% Al₂O₃ (dashed orange lines)⁴⁷. Velocity profiles of CaSiO₃ perovskite²⁸ (solid blue lines from modeling) and ferroprecilase^{27,43} (solid and open olive circles; olive lines show finite-strain fitting) at 300 K are plotted for comparisons. Uncertainties are smaller than symbols when not shown. c and d, VP and VS along an adiabat geotherm derived in our best-fit model (refer to Fig. 3 and Supplementary Fig. 9). Red lines: (Al,Fe)-bearing bridgmanite; olive lines: ferroprecilase; blue lines: CaSiO₃ perovskite. KD between bridgmanite and ferroprecilase with depth is taken from the literature¹⁰. The flattening in VS of ferroprecilase above ~45 GPa results from Fe preferentially partitioning into ferroprecilase across the spin crossover. Seismic profiles^{1,2} are plotted as dashed black and pink lines. Vertical ticks show one standard deviation ($\pm 1\sigma$) derived from error propagations.

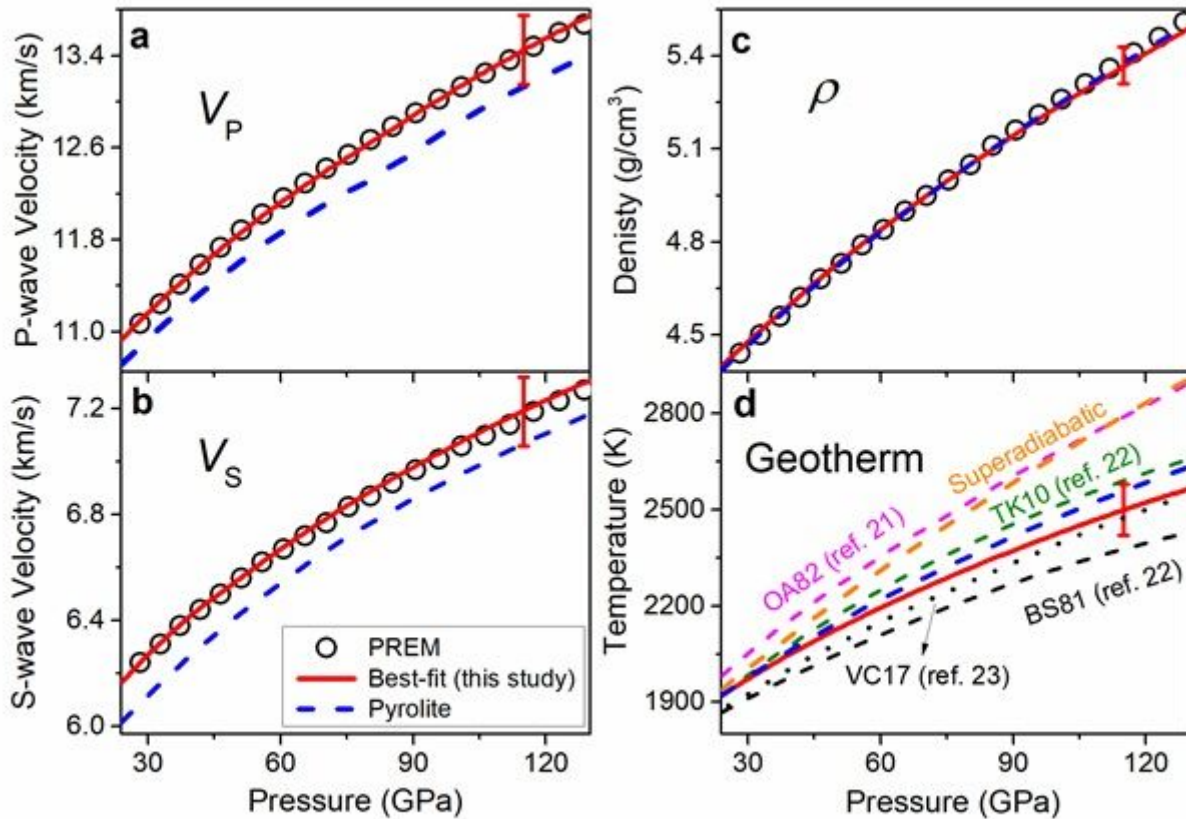


Figure 3

Modeled velocity, density, and temperature profiles of the lower mantle. a, V_P ; b, V_S ; c, ρ ; d, Geotherm. Solid red lines are our best-fits to PREM (open circles)¹ based on the fully internally-consistent thermoelastic model. Modeled results for a pyrolitic lower mantle¹⁰ are plotted as dashed blue lines. Our best-fit model shows the lower mantle is composed of $\sim 88.7(\pm 2.0)$ vol% bridgmanite, $\sim 4.3(\pm 2.0)$ vol% ferropericlase, and 7 vol% (fixed) CaSiO_3 perovskite. In d, solid red line shows the our derived adiabatic geotherm, whereas an adiabat for pyrolite (dashed blue line) and a superadiabatic geotherm (dashed orange line) with Bullen's parameter as ~ 0.8 are plotted for comparisons. Dashed olive²² and pink²¹ lines are literature models assuming a pyrolitic-whole-mantle convection and layered-mantle convection, respectively. Dashed black line²³ is an isentropic geotherm using entropies of mantle minerals based on the Debye model. Dotted black line is modeled for a chondritic composition from ab initio calculations²⁴. Vertical red ticks represent one standard deviation ($\pm 1\sigma$).

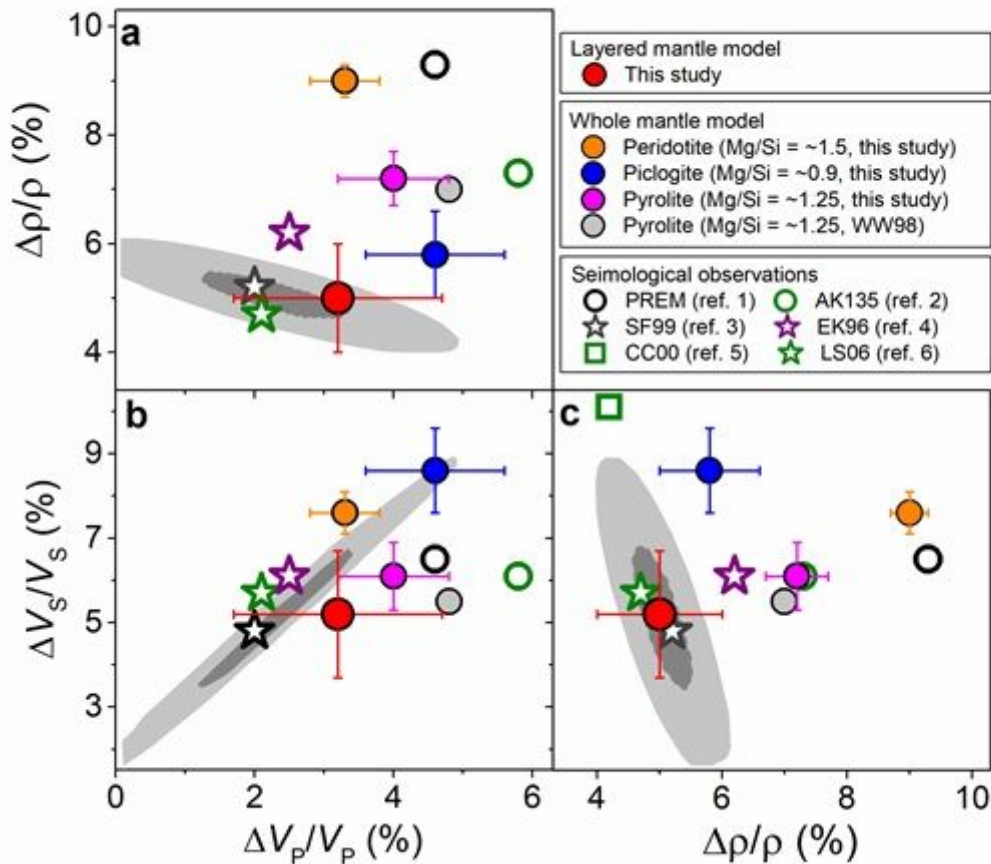


Figure 4

Comparisons of velocity and density jumps across the 660-km discontinuity between seismic observations and mantle compositional models. a, $\Delta\rho/\rho$ versus $\Delta V_P/V_P$; b, $\Delta V_S/V_S$ versus $\Delta V_P/V_P$; c, $\Delta V_S/V_S$ versus $\Delta\rho/\rho$. Two sets of compositional models are considered here: chemically layered mantle and chemically homogeneous whole mantle. Solid red circles are results for a chemically layered mantle with a pyrolitic transition zone⁸ and bridgmanite-predominant lower mantle in this study. Solid pink, orange, and blue circles are calculations for a chemically homogeneous whole mantle with Mg/Si of ~1.5 (peridotite⁵⁰), ~1.25 (pyrolite⁸), and ~0.9 (piclogite⁹), respectively. Literature results¹¹ for a pyrolitic whole mantle are plotted as solid gray circles (WW98). Errors of these models represent one standard deviation ($\pm 1\sigma$). Open symbols are from seismic observations: EK96 (open purple stars)⁴; LS06 (open olive stars)⁶; CC00 (open olive squares)⁵; SF99 (open black stars)³; PREM (open black circles)¹; AK135 (open olive circles)². Shaded dark and light gray areas are confidence ellipsoids within $\pm 1\sigma$ and $\pm 2\sigma$ limits, respectively, from Shearer and Flanagan³.

Supplementary Files

This is a list of supplementary files associated with this preprint. Click to download.

- [SupportingInformationNC0123.docx](#)